



Modeling Gamma-Ray Burst Afterglow Observations with an Off-axis Jet Emission

N. Fraija¹ , A. Galvan-Gamez¹ , B. Betancourt Kamenetskaia^{2,3} , M. G. Dainotti^{4,5} , S. Dichiara^{6,7} , P. Veres⁸ ,
R. L. Becerra⁹ , and A. C. Caligula do E. S. Pedreira¹

¹ Instituto de Astronomía, Universidad Nacional Autónoma de México, Circuito Exterior, C.U., A. Postal 70-264, 04510 Cd. de México, Mexico
nifraija@astro.unam.mx

² TUM Physics Department, Technical University of Munich, James-Frank-Str, D-85748 Garching, Germany

³ Max-Planck-Institut für Physik (Werner-Heisenberg-Institut), Föhringer Ring 6, 80805 Munich, Germany

⁴ National Astronomical Observatory of Japan, Division of Science, Mitaka, 2-chome, Japan

⁵ Space Science Institute, Boulder, CO, USA

⁶ Department of Astronomy, University of Maryland, College Park, MD 20742-4111, USA

⁷ Astrophysics Science Division, NASA Goddard Space Flight Center, 8800 Greenbelt Road, Greenbelt, MD 20771, USA

⁸ Center for Space Plasma and Aeronomic Research (CSPAR), University of Alabama in Huntsville, Huntsville, AL 35899, USA

⁹ Instituto de Ciencias Nucleares, Universidad Nacional Autónoma de México, Apartado Postal 70-264, 04510 México, CDMX, Mexico

Received 2022 January 19; revised 2022 April 8; accepted 2022 April 19; published 2022 December 6

Abstract

Gamma-ray bursts (GRBs) are fascinating extragalactic objects. They represent a fantastic opportunity to investigate unique properties not exhibited in other sources. Multiwavelength afterglow observations from some short- and long-duration GRBs reveal an atypical long-lasting emission that evolves differently from the canonical afterglow light curves favoring the off-axis emission. We present an analytical synchrotron afterglow scenario and the hydrodynamical evolution of an off-axis top-hat jet decelerated in a stratified surrounding environment. The analytical synchrotron afterglow model is shown during the coasting, deceleration (off- and on-axis emission), and post-jet break decay phases, and the hydrodynamical evolution is computed by numerical simulations showing the time evolution of the Doppler factor, the half-opening angle, the bulk Lorentz factor, and the deceleration radius. We show that numerical simulations are in good agreement with those derived with our analytical approach. We apply the current synchrotron model and successfully describe the delayed nonthermal emission observed in a sample of long and short GRBs with evidence of off-axis emission. Furthermore, we provide constraints on the possible afterglow emission by requiring the multiwavelength upper limits derived for the closest Swift-detected GRBs and promising gravitational-wave events.

Unified Astronomy Thesaurus concepts: [Gamma-ray bursts \(629\)](#); [Non-thermal radiation sources \(1119\)](#); [Interstellar medium \(847\)](#)

1. Introduction

Gamma-ray bursts (GRBs) are among the most powerful transient events in the universe. These events are detected as brief, nonrepeating flashes in the gamma-ray bands. Depending on the burst duration (from milliseconds to thousands of seconds), GRBs are commonly classified as short (sGRBs) and long (lGRBs) GRBs (Kouveliotou et al. 1993). An lGRB is associated with the core collapse (CC) of a dying massive star (Woosley 1993; Galama et al. 1998) that leads to a supernova (SN; Bloom et al. 1999; Woosley & Bloom 2006). At the same time, an sGRB is linked with the merger of a neutron star (NS) with a black hole (BH; Narayan et al. 1992) or two NSs (Duncan & Thompson 1992; Usov 1992; Thompson 1994; Metzger et al. 2011), as demonstrated by the historical gravitational-wave (GW) and electromagnetic detections of the GW170817 event (Abbott et al. 2017a).

On 2017 August 17, the joint detection of two messengers of the fusion of two NSs was achieved for the first time: the GW event (GW170817) by the Laser Interferometer Gravitational-Wave Observatory (LIGO) and VIRGO (Abbott et al. 2017a; von Kienlin et al. 2017) and the associated low-luminosity burst, GRB 170817A, by the Fermi Gamma-ray Space

Telescope (von Kienlin et al. 2017) and The International Gamma-Ray Astrophysics Laboratory (INTEGRAL; Savchenko et al. 2017). The results of this joint observation confirmed that NS fusion is a progenitor of sGRBs (Abbott et al. 2017). The association of GW170817A with the near host galaxy NGC 4993, located at a redshift of $z \simeq 0.01$ (Coulter et al. 2017; Margutti et al. 2017b), suggested the presence of a local population of low-luminosity bursts following the merger of two NSs (Abbott et al. 2017). Immediately, GRB 170817A was followed up by large observational campaigns covering the X-ray (Troja et al. 2017; Margutti et al. 2017a; Alexander et al. 2018; D’Avanzo et al. 2018; Haggard et al. 2018; Margutti et al. 2018), optical (Lyman et al. 2018; Margutti et al. 2018), and radio (Troja et al. 2017; Abbott et al. 2017b; Dobie et al. 2018; Mooley et al. 2018) bands, among others. In order to describe the delayed multiwavelength observations in timescales of days, synchrotron external-shock models radiated from off-axis top-hat jets (Alexander et al. 2017; Troja et al. 2017; Margutti et al. 2017b; Ioka & Nakamura 2018; Fraija et al. 2019a; Fraija et al. 2019b), radially stratified ejecta (Hotokezaka et al. 2018; Mooley et al. 2018; Fraija et al. 2019c), and structured jets (Kasliwal et al. 2017; Lazzati et al. 2018) were proposed. Later, analyses performed by Burns et al. (2018) and other authors (Fong et al. 2016; Burns et al. 2018; Troja et al. 2018) showed that GRB 150101B exhibits characteristics similar to GRB 170817A, in terms of its two-component structure and an undetected afterglow in a timescale



Original content from this work may be used under the terms of the [Creative Commons Attribution 4.0 licence](#). Any further distribution of this work must maintain attribution to the author(s) and the title of the work, journal citation and DOI.

of days followed by bright X-ray emission. Similar features in the multiwavelength afterglow have been found in GRB 080503 (Perley et al. 2009), GRB 140903A (Troja et al. 2016), and GRB 160821B (Stanbro & Meegan 2016; Lü et al. 2017). On the other hand, several searches for afterglow emission around the closest bursts ($\lesssim 200$ Mpc) reported by the Burst Alert Telescope (BAT) on board the Neil Gehrels Swift Observatory (Dichiara et al. 2020) and the GW events by the Advanced LIGO and Advanced VIRGO detectors (Abbott et al. 2021; The LIGO Scientific Collaboration et al. 2021) have been performed without success but have set multiwavelength upper limits.

The density profile of the medium surrounding a burst has been addressed previously in different contexts. For instance, for the case of SNe, Chevalier (1982) studied the interaction of an adiabatic flow in a circumstellar density profile for Type II SNe of the form $\propto r^{-2}$. Ever since, subsequent authors have adopted this proposal for modeling the circumstellar medium, and it has even been applied in the research of different SN types. Examples of such studies are those by Blondin et al. (1996), Soderberg et al. (2006), Kotak et al. (2004), and Chevalier (1984), among others. Nevertheless, a generalization of this power law has also been considered. A later study, Moriya & Tominaga (2012), showed that the diversity in the density slope of the surrounding environment might explain the spectral diversity of Type II luminous supernovae. To this effect, they proposed a wind density structure in the form $\propto r^{-k}$. They noticed that the ratio of the diffusion timescale in the optically thick region of the wind and the shock propagation timescale after the shock breakout strongly depend on the stratification parameter k , which led to differences in the spectral SN evolution. On the other hand, the requirement of a stratified environment condition has been proposed in some cases for modeling the multiwavelength afterglows, such as in work by Yi et al. (2013). The authors analyzed more than a dozen GRBs and concluded that the circumburst environment could be neither a homogeneous nor a stellar wind medium but something in between, with a general density distribution with a stratification parameter in the range $0.4 \leq k \leq 1.4$. A more recent example of an analysis that links SN and GRB emission with a stratified environment is the one by Izzo et al. (2020), in which the authors studied SN 2020bvc. They found an excellent agreement with the GRB-associated, broad-line Ic SN 1998bw; thus, it was categorized as a young broad-line Ic SN. They also noted that its X-ray light curve was consistent with simulations of an off-axis GRB afterglow in a stratified medium with $k = 1.5$; thus, this event represented the first case of an off-axis GRB discovered via its associated SN. It was later argued by Ho et al. (2020b), however, that such a model would predict an 8.5 GHz radio light curve several orders of magnitude more luminous than their measurements. Nevertheless, they stated that an off-axis jet could not be ruled out, and future radio observations would be needed.

In this work, we extend the analytical synchrotron afterglow scenario of the off-axis top-hat jet used to describe the multiwavelength afterglow observations in GRB 170817A (see Fraija & Lopez-Camara 2019b), adding several ingredients. Here we consider (i) the circumburst external medium as stratified with a profile density $\propto r^{-k}$ with k in the range of $0 \leq k < 3$, (ii) the synchrotron radiation in the self-absorption regime, (iii) the afterglow emission during the transition from

off-axis to on-axis before the lateral expansion phase (relativistic phase), (iv) the hydrodynamical evolution computed by numerical simulations, and (v) a fraction of electrons accelerated by the shock front. We apply the current model to describe the delayed nonthermal emission observed in GRB 080503, GRB 140903A, GRB 150101B, GRB 160821B, and SN 2020bvc and provide constraints on the possible afterglow emission using multiwavelength upper limits associated with the closest Swift-detected sGRBs and the promising GW events. This paper is arranged as follows. Section 2 presents the analytical synchrotron scenario and a hydrodynamical evolution of an off-axis top-hat jet decelerated in a stratified surrounding environment. In Section 3, we apply the proposed analytical model to describe the multiwavelength observations of a sample of bursts and provide constraints to other ones. In Section 4, we present our conclusions.

2. Off-axis Top-hat Model

2.1. Radiative Model

Accelerated electrons in forward-shock models are distributed in accordance with their Lorentz factors (γ_e) and described by the electron power index p as $N(\gamma_e)d\gamma_e \propto \gamma_e^{-p}d\gamma_e$ for $\gamma_m \leq \gamma_e$, where $\gamma_m = m_p/m_e g(p)\epsilon_e(\Gamma - 1)\zeta_e^{-1}$ is the minimum electron Lorentz factor, where Γ is the bulk Lorentz factor, m_p and m_e are the proton and electron mass, ϵ_e is the fraction of energy given to accelerate electrons, ζ_e denotes the fraction of electrons that were accelerated by the shock front (Fan & Piran 2006), and $g(p) = \frac{p-2}{p-1}$. The comoving magnetic field strength in the blast wave $B'^2/(8\pi) = \epsilon_B e$ is derived from the energy density $e = [(\hat{\gamma}\Gamma + 1)/(\hat{\gamma} - 1)](\Gamma - 1)n(r)m_p c^2$, with $\hat{\gamma}$ as the adiabatic index (Huang et al. 1999) and its respective fraction given to the magnetic field (ϵ_B). Hereafter, we adopt the unprimed and prime terms to refer to them in the observer and comoving frames, respectively. The term $\hat{\gamma}$ is the adiabatic index, and $n(r) = A_k r^{-k} = \frac{\dot{M}_W}{4\pi v_W} r^{-k}$, where v_W is the wind velocity, and \dot{M}_W is the mass-loss rate. The subindex k lies in the range $0 \leq k \leq 3$, where $k = 0$ is the constant-density medium ($A_0 = n$), and $k = 2$ is the stellar wind ejected by its progenitor ($A_2 \simeq A_W 3 \times 10^{35} \text{ cm}^{-1}$), where A_W is the density parameter. The cooling electron Lorentz factor is $\gamma_c = (6\pi m_e c/\sigma_T)(1 + Y)^{-1}\Gamma^{-1}B'^{-2}t^{-1}$, where σ_T is the cross section in the Thomson regime, and Y is the Compton parameter (Sari & Esin 2001; Wang et al. 2010; Fraija et al. 2019d, 2021). The synchrotron spectral breaks and the synchrotron radiation power per electron in the comoving frame are given by $\nu'_i = q_e/(2\pi m_e c)\gamma_i^2 B'$ and $P'_{\nu'_i m} \simeq \sqrt{3}q_e^3/(m_e c^2)B'$, respectively, hereafter with the subindexes $i = m$ and c for the characteristic and cooling break, and where the constants q_e and c are the elementary charge and the speed of light, respectively (e.g., see Sari et al. 1998; Fraija 2015). The synchrotron spectral breaks in the self-absorption regime are derived from $\nu'_{a,1} = \nu'_m \tau_{0,m}^{\frac{3}{5}}$, $\nu'_{a,2} = \nu'_m \tau_{0,m}^{\frac{2}{p+4}}$, and $\nu'_{a,3} = \nu'_c \tau_{0,c}^{\frac{3}{5}}$, with the optical depth given by $\tau_{0,i} \simeq \frac{5}{3-k} \frac{q_e n(r) r}{B' \gamma_i^5}$, where r is the shock radius (Panaitescu & Mészáros 1998). Considering the total number of emitting electrons $N_e = (\Omega/4\pi)n(r)\frac{4\pi}{3-k}r^3$ and also taking into account the transformation laws for the solid angle ($\Omega = \Omega'/\delta_D^2$), radiation power ($P_{\nu_m} = \delta_D/(1+z)P'_{\nu'_m}$), and spectral breaks

($\nu_i = \delta_D/(1+z)\nu'_i$), the maximum flux given by synchrotron radiation is

$$F_{\nu,\max} = \frac{(1+z)^2 \delta_D^3 N_e P' \nu'^m}{4\pi d_z^2}, \quad (1)$$

where $d_z = (1+z) \frac{c}{H_0} \int_0^z \frac{dz'}{\sqrt{\Omega_M(1+z')^3 + \Omega_\Lambda}}$ (Weinberg 1972) is the luminosity distance, $r = \delta_D/(1+z)\Gamma\beta ct$ is the shock radius, and $\delta_D = \frac{1}{\Gamma(1-\mu\beta)}$ is the Doppler factor, where $\mu = \cos \Delta\theta$; $\beta = v/c$, with v as the velocity of the material; and $\Delta\theta = \theta_{\text{obs}} - \theta_j$ is given by the viewing angle (θ_{obs}) and the half-opening angle of the jet (θ_j). We assume for the cosmological constants a spatially flat universe Λ CDM model with $H_0 = 69.6 \text{ km s}^{-1} \text{ Mpc}^{-1}$, $\Omega_M = 0.286$, and $\Omega_\Lambda = 0.714$ (Planck Collaboration et al. 2016).

2.2. Hydrodynamical Evolution versus Analytical Approach

2.2.1. Hydrodynamical Evolution

We consider the dynamical equations proposed by Huang et al. (1999, 2000). The dynamical evolution of the relativistic outflow into the circumburst medium can be described by

$$\begin{aligned} \frac{dr}{dt} &= \beta c \Gamma (\Gamma + \sqrt{\Gamma^2 - 1}), \\ \frac{dm}{dr} &= 2\pi (1 - \cos \theta_j) r^2 n m_p, \\ \frac{d\theta_j}{dt} &= \frac{c_s}{r} (\Gamma + \sqrt{\Gamma^2 - 1}), \\ \frac{d\Gamma}{dm} &= -\frac{\Gamma^2 - 1}{M_{\text{ej}} + \epsilon m + 2(1 - \epsilon)\Gamma m}, \end{aligned} \quad (2)$$

where $c_s = \sqrt{\hat{\gamma}(\gamma - 1)(\Gamma - 1)c^2/(1 + \hat{\gamma}(\Gamma - 1))}$ with $\hat{\gamma} \approx (4\Gamma + 1)/3\Gamma$, M_{ej} is the initial value of the ejected mass, and ϵ is the radiative efficiency, with $\epsilon = 0$ in the adiabatic regime and $\epsilon = 1$ in the fully radiative regime. The previous equations are consistent with the self-similar solution during the ultrarelativistic (Blandford–McKee solution; Blandford & McKee 1976) and Newtonian (Sedov–Taylor solution) phases, respectively, and consider the beaming effect (Rhoads 1999).

The observed quantities are integrated over the equal arrival time surface determined by Waxman (1997):

$$t = (1+z) \int \frac{dr}{\beta \Gamma c \delta_D} \equiv \text{const.} \quad (3)$$

2.2.2. Analytical Approach

During the coasting phase (before the deceleration phase), the relativistic outflow is not affected by the circumburst medium, so the bulk Lorentz factor is constant, $\Gamma_{\text{cp}} = \Gamma_0$, and the radius evolves as $r = c\beta_0 t / [(1+z)(1 - \beta_0\mu)]$, with $\beta_0 = \sqrt{\Gamma_0^2 - 1}/\Gamma_0$. During the deceleration phase, the relativistic outflow transfers a large amount of its energy to the circumstellar medium driving a forward shock. Considering the adiabatic evolution of the forward shock with an isotropic equivalent kinetic energy $E = \frac{4\pi}{3} m_p c^2 A_k r^3 \Gamma^2$ (Blandford–McKee solution; Blandford & McKee 1976) and a radial distance $r = c\beta_{\text{of}} t / [(1+z)(1 - \beta_{\text{of}}\mu)]$, the bulk Lorentz factor

evolves as

$$\begin{aligned} \Gamma_{\text{of}} &= \left(\frac{3}{4\pi m_p c^{5-k}} \right)^{\frac{1}{2}} (1+z)^{-\frac{k-3}{2}} \\ &\times (1 - \beta \cos \Delta\theta)^{-\frac{(k-3)}{2}} A_k^{-\frac{1}{2}} E^{\frac{1}{2}} t^{\frac{k-3}{2}}, \end{aligned} \quad (4)$$

with $\beta_{\text{of}} = \sqrt{\Gamma_{\text{of}}^2 - 1}/\Gamma_{\text{of}}$. The deceleration timescale t_{dec} can be defined using Equation (4). As the bulk Lorentz factor becomes $\Gamma \simeq 1/\Delta\theta$, the observed flux becomes in our field of view. During the on-axis emission, the bulk Lorentz factor in the adiabatic regime evolves as

$$\begin{aligned} \Gamma_{\text{on}} &= \left(\frac{3}{(2c)^{5-k} \pi m_p} \right)^{\frac{1}{8-2k}} \\ &\times (1+z)^{-\frac{k-3}{8-2k}} A_k^{-\frac{1}{8-2k}} E^{\frac{1}{8-2k}} t^{\frac{k-3}{8-2k}}, \end{aligned} \quad (5)$$

with the radius $r \simeq 2\beta_{\text{on}} \Gamma_{\text{on}}^2 ct / (1+z)$ and $\beta_{\text{on}} = \sqrt{\Gamma_{\text{on}}^2 - 1}/\Gamma_{\text{on}}$, before the outflow enters the post-jet break decay phase ($\Gamma \simeq 1/\theta_j$). During the post-jet break decay phase, the bulk Lorentz factor evolves as

$$\begin{aligned} \Gamma_{\text{le}} &= \left(\frac{3}{(2c)^{5-k} \pi m_p} \right)^{\frac{1}{6-2k}} (1+z)^{-\frac{k-3}{6-2k}} \\ &\times A_k^{-\frac{1}{6-2k}} E^{\frac{1}{6-2k}} \theta_j^{\frac{1}{3-k}} t^{\frac{k-3}{6-2k}}, \end{aligned} \quad (6)$$

with the shock's radius and velocity given by $r \simeq 2\beta_{\text{le}} \Gamma_{\text{le}}^2 ct / (1+z)$ and $\beta_{\text{le}} = \sqrt{\Gamma_{\text{le}}^2 - 1}/\Gamma_{\text{le}}$, respectively. We summarize the evolution of the bulk Lorentz factor as

$$\Gamma \propto \begin{cases} t^0, & t < t_{\text{dec}}, \\ t^{\frac{k-3}{2}}, & t_{\text{dec}} \leq t \leq t_{\text{pk}}, \\ t^{\frac{k-3}{8-2k}}, & t_{\text{pk}} \leq t \leq t_{\text{br}}, \\ t^{\frac{k-3}{6-2k}}, & t_{\text{br}} \leq t, \end{cases} \quad (7)$$

where the respective timescales are

$$\begin{aligned} t_{\text{dec}} &= t_{\text{dec},0} (1+z) (1 - \beta \cos \Delta\theta)^2 A_k^{-\frac{1}{k-3}} E^{\frac{1}{k-3}} \Gamma^{-\frac{2}{3-k}}, \\ t_{\text{pk}} &= t_{\text{pk},0} (1+z) A_k^{\frac{1}{k-3}} E^{-\frac{1}{k-3}} \Delta\theta^{-\frac{8-2k}{k-3}}, \\ t_{\text{br}} &= t_{\text{br},0} (1+z) A_k^{-\frac{1}{3-k}} E^{\frac{1}{3-k}} \theta_j^2, \end{aligned} \quad (8)$$

with $t_{\text{dec},0} = (3/4\pi m_p c^{5-k})^{\frac{1}{3-k}}$ and $t_{\text{pk},0} = t_{\text{br},0} = (3/(2c)^{5-k} \pi m_p)^{\frac{1}{3-k}}$. It is worth noting that the afterglow emission enters the observer's field of view at t_{pk} . For instance, the bulk Lorentz factor in a constant-density medium evolves first as $\propto t^0$ (Sari & Piran 1999), then $t^{-\frac{3}{2}}$ (Nakar & Piran 2018; Fraija & Lopez-Camara 2019b), $t^{-\frac{3}{8}}$ (Sari et al. 1998), and, finally, $t^{-\frac{1}{2}}$ (Sari et al. 1999), as expected.

The minimum and cooling electron Lorentz factors, the spectral breaks, the maximum flux, and the synchrotron light curves during the coasting, deceleration (off- and on-axis), and post-jet break decay phases are shown in the Appendix and Tables 1–3.

Table 1
Evolution of the Synchrotron Light Curves ($F_\nu \propto t^{-\alpha} \nu^{-\beta}$) from an Off-axis Outflow Decelerated in a Stratified Environment

	Coasting Phase	Deceleration Phase (Off-axis Afterglow)	Deceleration Phase (On-axis Afterglow)	Post– Jet Break Phase	
β	α	α	α	α	
$\nu_{a,3} < \nu_c < \nu_m$					
$\nu < \nu_{a,3}$	-2	$-(1+k)$	-4	$-\frac{4}{4-k}$	-1
$\nu_{a,3} < \nu < \nu_c$	$-\frac{1}{3}$	$\frac{6k-11}{3}$	$\frac{8k-17}{3}$	$\frac{3k-2}{3(4-k)}$	1
$\nu_c < \nu < \nu_m$	$\frac{1}{2}$	$\frac{3k-8}{4}$	$\frac{9k-26}{4}$	$\frac{1}{4}$	1
$\nu_m < \nu$	$\frac{p}{2}$	$\frac{k(p+2)-8}{4}$	$\frac{2(3p-16)-(p-10)k}{4}$	$\frac{3p-2}{4}$	p
$\nu_{a,1} < \nu_m < \nu_c$					
$\nu < \nu_{a,1}$	-2	-2	-2	$-\frac{2}{4-k}$	0
$\nu_{a,1} < \nu < \nu_m$	$-\frac{1}{3}$	$\frac{4k-9}{3}$	$\frac{8k-21}{3}$	$\frac{k-2}{4-k}$	$\frac{1}{3}$
$\nu_m < \nu < \nu_c$	$\frac{p-1}{2}$	$\frac{k(p+5)-12}{4}$	$\frac{6(p-5)-(p-11)k}{4}$	$-\frac{12(1-p)+k(3p-5)}{4(4-k)}$	p
$\nu_c < \nu$	$\frac{p}{2}$	$\frac{k(p+2)-8}{4}$	$\frac{2(3p-16)-(p-10)k}{4}$	$\frac{3p-2}{4}$	p
$\nu_m < \nu_{a,2} < \nu_c$					
$\nu < \nu_m$	-2	-2	-2	$-\frac{2}{4-k}$	0
$\nu_m < \nu < \nu_{a,2}$	$-\frac{5}{2}$	$-\frac{8+k}{4}$	$\frac{k-14}{4}$	$\frac{3k-20}{4(4-k)}$	-1
$\nu_{a,2} < \nu < \nu_c$	$\frac{p-1}{2}$	$\frac{k(p+5)-12}{4}$	$\frac{6(p-5)-(p-11)k}{4}$	$-\frac{12(1-p)+k(3p-5)}{4(4-k)}$	p
$\nu_c < \nu$	$\frac{p}{2}$	$\frac{k(p+2)-8}{4}$	$\frac{2(3p-16)-(p-10)k}{4}$	$\frac{3p-2}{4}$	p

Table 2
Closure Relations of Synchrotron Radiation from Off-axis Afterglow Model in a Stratified Environment

	Coasting Phase	Deceleration Phase (Off-axis Afterglow)	Deceleration Phase (On-axis Afterglow)	Post–Jet Break Phase	
$\nu_{a,3} < \nu_c < \nu_m$					
$\nu < \nu_{a,3}$	-2	$\frac{(k+1)\beta}{2}$	2β	$\frac{\beta}{2}$	
$\nu_{a,3} < \nu < \nu_c$	$-\frac{1}{3}$	$(11-6k)\beta$	$(17-8k)\beta$	$-\frac{(2-3k)\beta}{4-k}$	-3β
$\nu_c < \nu < \nu_m$	$\frac{1}{2}$	$\frac{(3k-8)\beta}{2}$	$\frac{(9k-26)\beta}{2}$	$\frac{\beta}{2}$	2β
$\nu_m < \nu$	$\frac{p}{2}$	$\frac{(\beta+1)k-4}{2}$	$\frac{(6-k)\beta+5k-16}{2}$	$\frac{3\beta-1}{2}$	2β
$\nu_{a,1} < \nu_m < \nu_c$					
$\nu < \nu_{a,1}$	-2	β	β	$\frac{\beta}{4-k}$	0
$\nu_{a,1} < \nu < \nu_m$	$-\frac{1}{3}$	$(9-4k)\beta$	$(21-8k)\beta$	$\frac{3(2-k)\beta}{4-k}$	$-\beta$
$\nu_m < \nu < \nu_c$	$\frac{p-1}{2}$	$\frac{k(\beta+3)-6}{2}$	$\frac{(6-k)\beta+5k-12}{2}$	$\frac{3(4-k)\beta+k}{2(4-k)}$	$2\beta+1$
$\nu_c < \nu$	$\frac{p}{2}$	$\frac{(\beta+1)k-4}{2}$	$\frac{(6-k)\beta+5k-16}{2}$	$\frac{3\beta-1}{2}$	2β
$\nu_m < \nu_{a,2} < \nu_c$					
$\nu < \nu_m$	-2	β	β	$\frac{\beta}{4-k}$	0
$\nu_m < \nu < \nu_{a,2}$	$-\frac{5}{2}$	$\frac{(k+8)\beta}{10}$	$\frac{(14-k)\beta}{10}$	$\frac{(20-3k)\beta}{10(4-k)}$	$\frac{2\beta}{5}$
$\nu_{a,2} < \nu < \nu_c$	$\frac{p-1}{2}$	$\frac{k(\beta+3)-6}{2}$	$\frac{(6-k)\beta+5k-12}{2}$	$\frac{3(4-k)\beta+k}{2(4-k)}$	$2\beta+1$
$\nu_c < \nu$	$\frac{p}{2}$	$\frac{(\beta+1)k-4}{2}$	$\frac{(6-k)\beta+5k-16}{2}$	$\frac{3\beta-1}{2}$	2β

2.3. Comparison of our Model with Previous Simulations

Figure 1 presents examples of the time evolution of the Doppler factor, the half-opening angle, the bulk Lorentz factor, and the deceleration radius, all in a constant circumburst medium ($k=0$). The solid lines characterize the numerical simulations, while the dashed lines stand in for the theoretical

approximations, which are detailed in the [Appendix](#). Lines in black correspond to quantities observed off-axis, and lines in gray correspond to the ones observed on-axis.

For the case of δ_D , the upper left panel shows an excellent agreement between the simulations and the model at early times up to $t_{\text{obs}} \approx 10^2$ s. After this point, there are very slight

Table 3
Proportionality Constants of the Relevant Quantities in the Synchrotron Model

	$k = 0$	$k = 1.0$	$k = 1.5$	$k = 2.0$	$k = 2.5$
A_k	1 cm^{-3}	$1.4 \times 10^{28} \text{ cm}^{-2}$	$2.8 \times 10^{36} \text{ cm}^{-\frac{3}{2}}$	$2.8 \times 10^{44} \text{ cm}^{-1}$	$1.4 \times 10^{51} \text{ cm}^{-\frac{1}{2}}$
Coasting Phase					
$\gamma_m^0 (\times 10^3)$	9.15	9.15	9.15	9.15	9.15
γ_c^0	1.60×10^5	1.03×10	1.85	6.65×10^{-1}	4.77
$\nu_{a,1}^0 (\text{Hz})$	4.47×10^{-8}	1.23	2.72×10	1.72×10^2	4.96
$\nu_{a,2}^0 (\text{Hz})$	5.46×10^{-3}	2.66	8.30	1.64×10	4.44
$\nu_{a,3}^0 (\times 10^{-3} \text{ Hz})$	7.80×10^{-4}	1.39	5.51	1.25×10	2.59
$\nu_m^0 (\times 10^4 \text{ Hz})$	1.62×10^{-2}	1.74	4.12	6.87	2.57
$\nu_c^0 (\times 10^{-3} \text{ Hz})$	4.93×10^7	2.22×10	1.69	3.63×10^{-1}	6.97
$F_{\text{max}}^0 (\times 10^3 \text{ mJy})$	6.57×10^{-8}	8.22×10^{-2}	1.08	5.04	2.62×10^{-1}
Deceleration Phase (Off-axis)					
$\gamma_m^0 (\times 10)$	7.56	3.48	6.59	2.06×10	1.96×10^2
$\gamma_c^0 (\times 10^4)$	2.80	4.08×10^{-1}	1.98	8.44×10	9.33×10^6
$\nu_{a,1}^0 (\times 10^{-6} \text{ Hz})$	7.55×10^{-2}	1.80	1.35×10^{-1}	2.45×10^{-4}	6.72×10^{-13}
$\nu_{a,2}^0 (\times 10^{-5} \text{ Hz})$	1.00	1.93	1.13	2.47×10^{-1}	1.05×10^{-3}
$\nu_{a,3}^0 (\times 10^{-5} \text{ Hz})$	2.80	2.11×10	4.04	1.00×10^{-1}	3.20×10^{-6}
$\nu_m^0 (\times 10^{-6} \text{ Hz})$	3.03	1.20	2.58	7.04	8.87
$\nu_c^0 (\times 10^{-1} \text{ Hz})$	4.17	1.65×10^{-1}	2.32	1.18×10^3	2.01×10^{11}
$F_{\text{max}}^0 (\times 10 \text{ mJy})$	4.10	7.66	4.59	7.02×10^{-1}	1.39×10^{-4}
Deceleration Phase (On-axis)					
$\gamma_m^0 (\times 10^3)$	2.83	1.43	1.51	1.96	8.19
$\gamma_c^0 (\times 10^2)$	3.95×10	1.36	1.78	6.32	1.28×10^4
$\nu_{a,1}^0 (\times 10^{-3} \text{ Hz})$	1.80×10^{-2}	6.77	4.23	4.54×10^{-1}	1.02×10^{-6}
$\nu_{a,2}^0 (\times 10^{-2} \text{ Hz})$	5.74×10^{-1}	3.25	2.83	1.47	3.78×10^{-2}
$\nu_{a,3}^0 (\times 10^{-4} \text{ Hz})$	2.51×10^{-1}	6.44	4.98	1.47	1.58×10^{-3}
$\nu_m^0 (\text{Hz})$	3.17	3.10	3.11	3.14	3.21
$\nu_c^0 (\times 10^{-2} \text{ Hz})$	6.15×10^2	2.81	4.31	3.28×10	7.79×10^6
$F_{\text{max}}^0 (\times 10^3 \text{ mJy})$	1.14×10^{-1}	1.69	1.36	4.95×10^{-1}	1.68×10^{-3}
Post-Jet Break Decay Phase					
$\gamma_m^0 (\times 10)$	4.68	1.95	4.03	1.69×10	1.74×10^2
$\gamma_c^0 (\times 10^4)$	3.92	4.89×10^{-1}	2.71	1.52×10^2	2.32×10^7
$\nu_{a,1}^0 (\times 10^{-8} \text{ Hz})$	3.40	9.82×10	6.22	7.57×10^{-3}	1.20×10^{-11}
$\nu_{a,2}^0 (\times 10^{-6} \text{ Hz})$	4.80	9.38	5.43	1.21	4.48×10^{-3}
$\nu_{a,3}^0 (\times 10^{-5} \text{ Hz})$	2.85	2.47×10	4.19	6.83×10^{-2}	1.60×10^{-6}
$\nu_m^0 (\times 10^{-7} \text{ Hz})$	6.06	2.10	5.05	2.37×10	3.13×10
$\nu_c^0 (\times 10^{-1} \text{ Hz})$	4.25	1.32×10^{-1}	2.29	1.93×10^3	5.55×10^{11}
$F_{\text{max}}^0 (\text{mJy})$	2.14×10	4.28×10	2.41×10	4.97	7.81×10^{-4}

variations between both solutions, specifically in the steepness of the rise and fall of this quantity. The numerical simulation predicts a sharper peak, while the theoretical approximation anticipates a wider profile. Despite this slight difference, both curves drop in parallel, showing that their delinquent behavior follows the same power law. In the case of the half-opening angle θ_j (lower left panel), as in the case of δ_D , the early-time evolution is the same between both curves. The difference in their behavior is first made apparent at $t_{\text{obs}} \approx 10^2$ s. At this time, the theoretical solution presents a faster rise than the simulation. The initial variation between both curves keeps increasing and becomes substantial at times $\geq 10^6$ s.

The upper right panel compares the bulk Lorentz factors when the emission is off- and on-axis. For the off-axis case, the

same features mentioned in the last two panels are repeated, namely, perfect agreement at early times and variations at late times. However, the on-axis emission is different, as there are slight differences initially, but both solutions tend to be the same as time progresses. Finally, the lower right panel presents the shock's radius for the on- and off-axis cases. For the on-axis curves, the simulation and theoretical approximation differ early, but they unite late. There is also a difference in their shapes at the beginning, as the theoretical curve is a straight line, which corresponds to a single power law. At the same time, the simulation shows that there is a transition from a flatter curve to a steeper one. The case of the off-axis emission presents similar differences. In general, the simulation and the theoretical variables exhibited in Figure 1 are in good agreement.

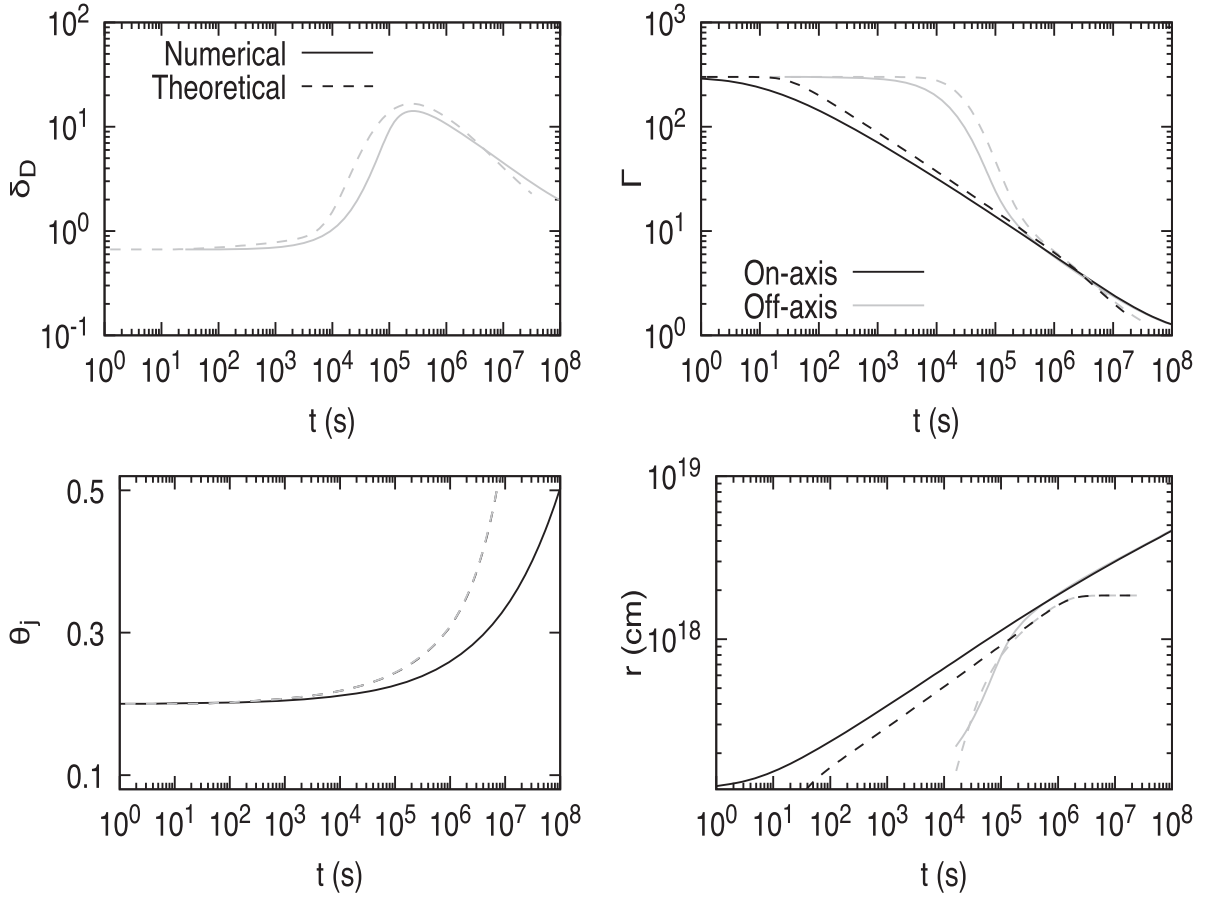


Figure 1. Comparison of numerical simulations (solid lines) and a theoretical approach (dashed lines) of the Doppler factor (δ_D), the jet’s opening angle θ_j , the bulk Lorentz factor (Γ), and the deceleration radius (r), all of them evolving in a constant circumburst medium. Variables observed off- and on-axis are in black and gray, respectively. The parameters $E = 10^{54}$ erg, $n = 1.0 \text{ cm}^{-3}$, $\Delta\theta = 5.972$, and $\Gamma_0 = 300$ are used.

2.4. Analysis and Description of the Synchrotron Light Curves

The analytical synchrotron afterglow model during the coasting, deceleration (off- and on-axis emission), and post-jet break decay phases are shown in the [Appendix](#). [Table 1](#) shows the evolution of the synchrotron light curves, and [Table 2](#) shows the closure relations of synchrotron radiation as a function of k during the coasting, deceleration (off- and on-axis emission), and post-jet break decay phases in the stratified environment. We can note in both tables that a break is expected around the transition time between fast- and slow-cooling regimes during the deceleration phase when the afterglow emission is seen off-axis but not during another phase.

Figures 2 and 3 show the predicted synchrotron light curves produced by the deceleration of the off-axis top-hat jet in the circumburst medium described by a density profile with $k = 0, 1.0, 1.5,$ and $2.0,$ respectively. From top to bottom, the panels correspond to radio wavelength at 6 GHz, optical at the R band, and X-rays at 1 keV for typical values of GRB afterglow.¹⁰ These figures display that, regardless of the viewing angle, the X-ray, optical, and radio fluxes increase gradually, reach the maximum value, and, finally, begin to decrease. It can be observed that as the viewing angle increases, the maximum value moves to later times. For the chosen parameters, in most

cases, the maximum value lies in the range of $(10^{-1}-10^2)$ days for $0^\circ \leq \theta_{\text{obs}} \leq 60^\circ$. This is different, however, when the medium is like a stellar wind, as the right column of [Figure 3](#) shows that the maximum happens later, namely, in the range of $(10^{-1}-10^4)$ days. [Figures 2](#) and [3](#) show that the bump is less evident in the light curves with $1.0 \leq k \leq 2.0$. Then, a clear rebrightening in a timescale from days to weeks with GW detection could be associated with the deceleration of the off-axis jet launched by a binary neutron star or BH-NS merger. The synchrotron fluxes in all of these panels lie in the slow-cooling regime, although for a different set of parameters with values (for instance, the equivalent kinetic energy $E = 10^{54}$ erg, the uniform-density medium $n \approx 1 \text{ cm}^{-3}$, and the equipartition parameters $\varepsilon_e = 0.1$ and $\varepsilon_B = 10^{-4}$), these would lie in the fast-cooling regime.

[Table 4](#) shows the evolution of the density parameter in each cooling condition of the synchrotron afterglow model. For instance, the synchrotron light curve as a function of the density parameter in the cooling condition $\nu_{a,1} < \nu_m < \nu_c$ is given by $F_\nu: \propto A_k^{\alpha_k}$, with $\alpha_k = \frac{p+5}{4}, \frac{11-p}{4}, \frac{2}{4-k}$, and $\frac{3-p}{4(3-k)}$, for the coasting, deceleration (off- and on-axis), and post-jet break decay phases, respectively. Any transition between a stratified environment and density-constant medium could be detected during the post-jet break and deceleration phases when the afterglow emission (for this cooling condition) is seen on-axis but not off-axis. [Table 4](#) shows that in general, during the coasting phase and the deceleration phase when the afterglow

¹⁰ $E = 10^{54}$ erg, $\varepsilon_B = 10^{-4}$, $\varepsilon_e = 10^{-1}$, $\zeta_e = 1.0$, and $d_z = 1$ Gpc. Henceforth, we adopt the convention $Q_x = Q/10^x$ in cgs units for all variables except angles. For angles, we adopt the convention $Q_x = Q/x$ in degrees.

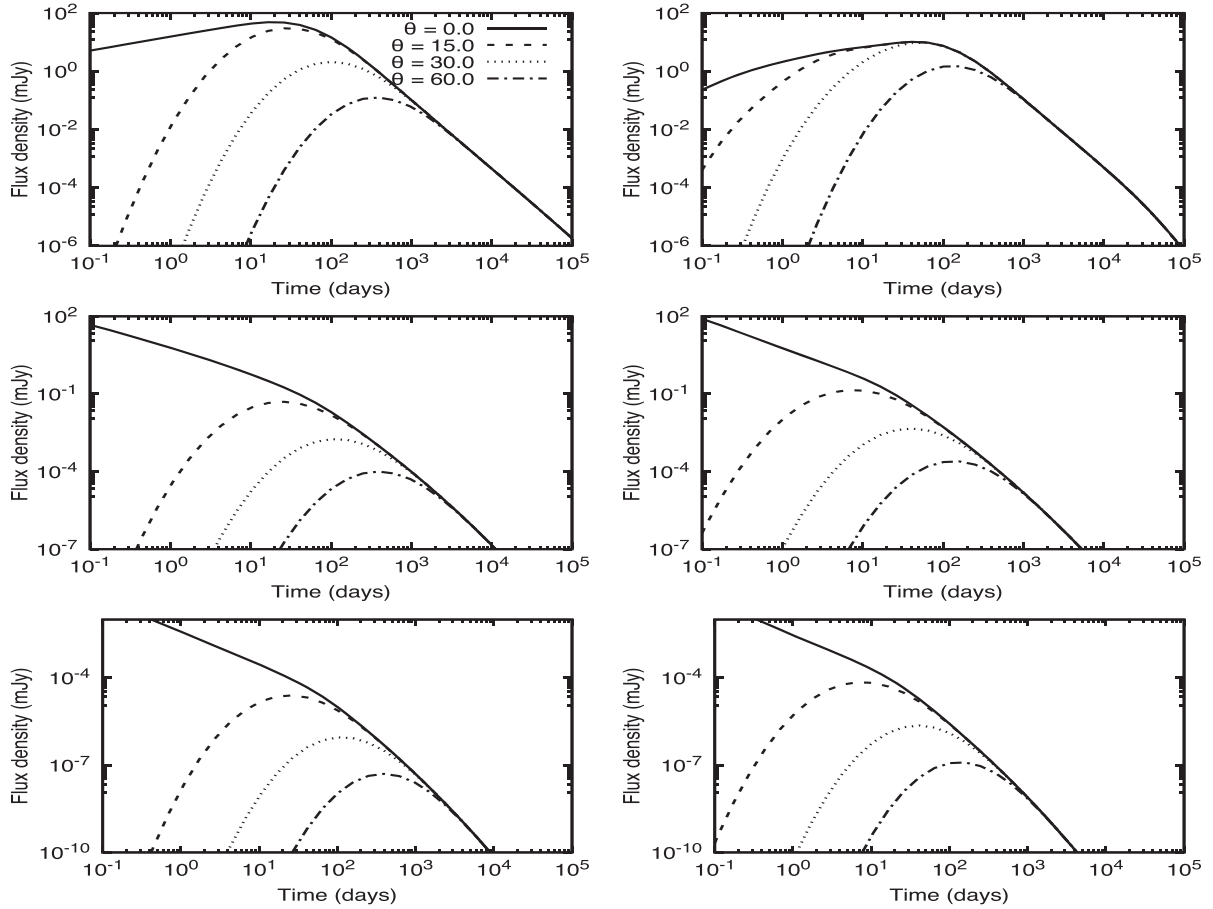


Figure 2. Synchrotron light curves generated by the deceleration of the off-axis jet for $k = 0$ (left) and 1 (right). Panels from top to bottom correspond to the radio (1.6 GHz), optical (R), and X-ray (1 keV) bands, respectively. The parameters $E = 10^{51}$ erg, $\epsilon_B = 10^{-4}$, $\epsilon_e = 10^{-1}$, $\Gamma = 300$, $p = 2.2$, $\zeta_e = 1.0$, and $d_c = 6.6$ Gpc are used.

emission seems off-axis, a change of density profile would not produce a significant variation in the flux. Table 4 displays that synchrotron fluxes do not depend on the density parameter when they are observed at the lowest-energy ($\nu < \min\{\nu_{a,1}, \nu_{a,2}, \nu_{a,3}\}$) and highest-energy ($\max\{\nu_m, \nu_c\} < \nu$) frequencies when the afterglow emission is seen off- and on-axis, respectively. During the post-jet break phase, any transition between a stratified environment and density-constant medium will be better observed in low-energy frequencies, such as radio wavelengths.

The uniform medium with constant density is expected for sGRBs associated with binary compact objects, and the stratified medium with nonconstant density is expected for IGRBs related to massive stars with different evolution at the end of their lives (Ramirez-Ruiz et al. 2005; van Marle et al. 2006). For instance, an external stratified medium with $0.4 \leq k \leq 1.4$ was found by Yi et al. (2013) after modeling the afterglow emission in a GRB example, and a density profile with $k > 2$ was reported by Kumar et al. (2008) after studying the accretion of the stellar envelope by a BH as the possible origin of the plateau phase in X-ray light curves.

Giblin et al. (1999) analyzed the prompt gamma-ray emission in the BATSE¹¹-detected burst GRB 980923. The light curve exhibited a main prompt episode lasting ~ 32 s, followed by a smooth emission tail that lasted ~ 390 s. The

authors found that the spectrum in the smooth tail evolved as the synchrotron cooling break $t^{-0.52 \pm 0.12}$, concluding that the gamma-ray emission was associated with the afterglow evolution, and also that it had begun during the prompt gamma-ray episode. Afterward, spectra analyses of GRB tails were done to identify early afterglows (Barthelmy et al. 2005; Yamazaki et al. 2006). We could identify the off-axis synchrotron emission from an off-axis outflow analyzing the spectral break evolution. In this case, the spectral breaks of the synchrotron radiation generated from the deceleration of the off-axis jet in the relativistic phase evolve as a $\nu_m \propto t^{-\frac{6-k}{3}}$ and $\nu_c \propto t^{\frac{2+k}{2}}$, respectively. For instance, with $k = 1$, the characteristic and cooling breaks evolve as $\nu_m \propto t^{-\frac{5}{3}}$ and $\nu_c \propto t^{\frac{3}{2}}$, respectively, which are fully different from the breaks that evolve when the afterglow emission is on-axis (e.g., $\nu_m \propto t^{-\frac{3}{2}}$ and $\nu_c \propto t^{-\frac{1}{6}}$).

3. A Sample of Some Bursts with Evidence of Off-axis Afterglow Emission

3.1. Multiwavelength Observations

GRB 080503—On 2008 May 3 at 12:26:13 UTC, the Swift-BAT instrument detected and triggered on the short burst GRB 080503 (Mao et al. 2008; Ukwatta et al. 2008). The prompt episode was evaluated in the 15–150 keV energy range and reported with a duration of 0.32 ± 0.07 s, while its observed

¹¹ Burst and Transient Source Experiment.

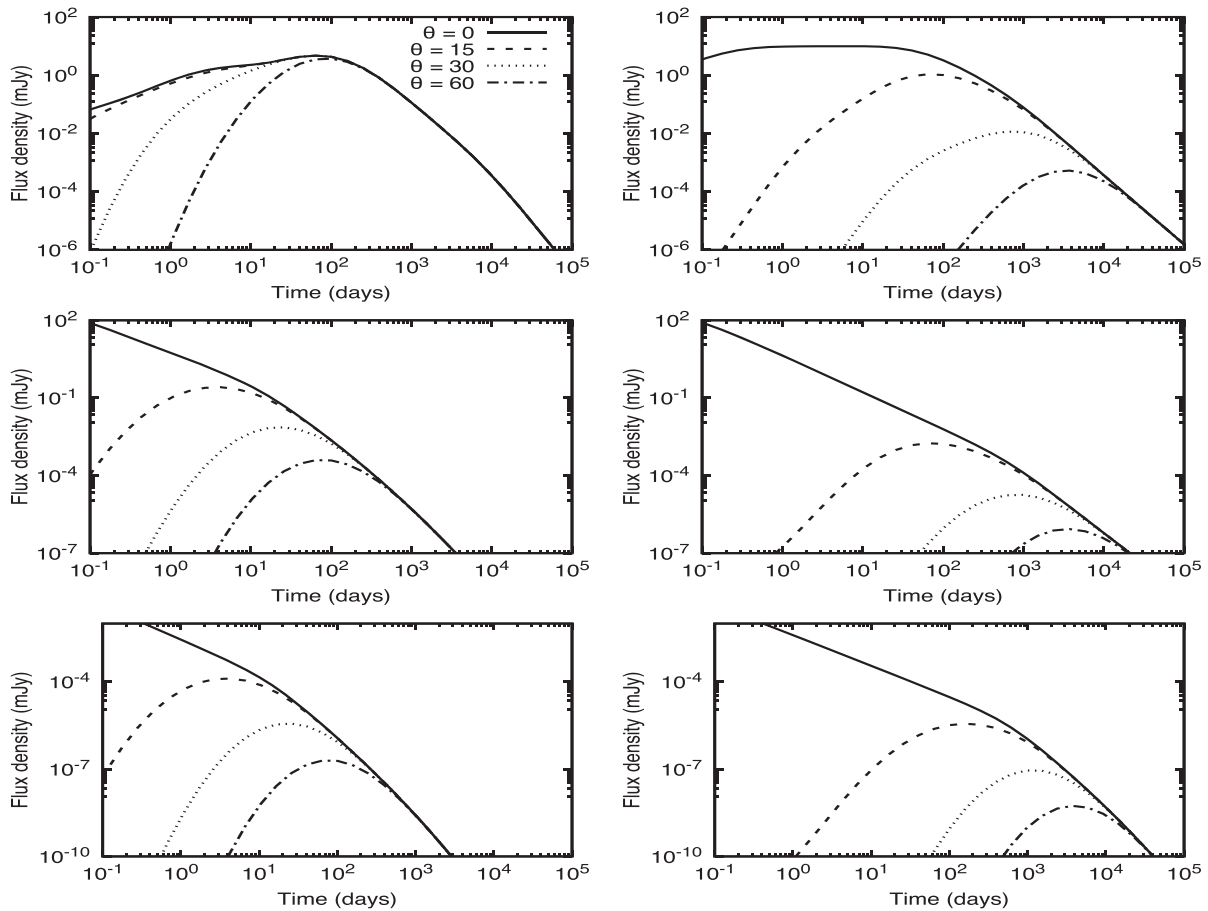


Figure 3. Synchrotron light curves generated by the deceleration of the off-axis jet for $k = 1.5$ (left) and 2 (right). Panels from top to bottom correspond to the radio (1.6 GHz), optical (R), and X-ray (1 keV) bands, respectively. The parameters $E = 10^{51}$ erg, $\epsilon_B = 10^{-4}$, $\epsilon_e = 10^{-1}$, $\Gamma = 300$, $p = 2.2$, $\zeta_e = 1.0$, and $d_c = 6.6$ Gpc are used.

flux was measured to be $(1.2 \pm 0.2) \times 10^{-7}$ erg cm $^{-2}$ s $^{-1}$. The Swift X-ray Telescope (XRT) instrument and Chandra ACIS-S satellite also performed subsequent observations in the X-ray band (Guidorzi & Mao 2008; Perley et al. 2009). For the case of Swift-XRT, it took data on the burst in the time frame from ~ 82 s to 1 day after the initial Swift-BAT trigger. On the other hand, Chandra measured the burst throughout two observational campaigns, the first from 2008 May 7 (19:18:23 UTC) to 8 (04:09:59 UTC), during which an X-ray flux was detected that coincided with the location of the optical afterglow. The second campaign took place from 2008 May 25 (18:11:36) to 26 (03:04:28), during which the X-ray source was monitored. There was a lack of detection, but constraining limits were provided. Several efforts were also taken to monitor this burst in the optical energy range. Observations and upper limits were obtained with the Swift Ultra-Violet Optical Telescope (UVOT) instrument (Brown & Mao 2008); the Hubble Space Telescope (HST) using the Wide-Field Planetary Camera in the F606W, F450W, and F814W bands (Bloom et al. 2008; Perley et al. 2008b, 2008c, 2008f); and the Keck I telescope equipped with LRIS (Perley et al. 2008e). The Gemini-N observatory also observed the burst using the Multi-Object Spectrograph through the g , r , i , and z optical bands and NIRI through the K_s band (Perley et al. 2008a; Bloom & Perley 2008). Regarding the radio energy band, the Karl G. Jansky Very Large Array (VLA) was used to observe GRB 080503 at a frequency of 8.46 GHz

without any detection but providing a 3σ upper limit (Frail & Chandra 2008).

GRB 140903A—The Swift-BAT detected GRB 140903A at 15:00:30 UT on 2014 September 14 (Cummings et al. 2014). This burst was located with coordinates R.A. = $238^\circ 036$, decl. = $+27^\circ 578$ (J2000). The BAT light curve exhibited a peak with a duration of 0.45 s (Cummings 2014). The XRT instrument began observing the position of this burst 59 s after the BAT trigger and monitored the X-ray afterglow until this emission faded below the detector sensitivity threshold. The MAXI-GSC observed the position reported by BAT 12 s after the trigger. Although no object was detected, upper limits were derived at the 4–10 keV energy range. The Chandra satellite began observing the X-ray afterglow ~ 2.7 s after the BAT trigger (Sakamoto et al. 2014). This burst was observed in the optical r band (20.4 ± 0.5 mag) by the 2 m Faulkes Telescope North ~ 15.6 hr after the BAT trigger (Dichiara et al. 2014). The Nordic Optical Telescope observed the field of this burst, reporting an optical emission of 20.1 ± 0.5 and 16.1 ± 0.3 mag in the R and H bands. Cucchiara et al. (2014) identified a strong absorption doublet feature of the wavelengths in the range of 795.4 and 796.5 nm (Cucchiara et al. 2014). These lines were associated with NaID in absorption and $H\beta$ in emission at the usual redshift of $z = 0.351$. Later, the detection of optical variability, together with a coincident radio detection (Fong 2014), confirmed the host association of this redshift (Cenko et al. 2014).

GRB 150101B—The Swift-BAT and Fermi Gamma-Ray Monitor (GBM) detected GRB 150101B at 15:23:35 and 15:24:34.468 UT on 2015 January 1, respectively (Cummings 2015; Stanbro 2015; Burns et al. 2018). Data analysis of Swift-BAT revealed a bright source, constraining the location at R. A. = 188°044, decl. = $-10^{\circ}956$ (J2000). The γ -ray pulse in the 15–150 keV band consisted of a single pulse with a duration and fluence of 0.012 ± 0.001 s and $F_{\gamma} = (6.1 \pm 2.2) \times 10^{-8}$ erg cm $^{-2}$, respectively (Lien et al. 2016). Recently, Burns et al. (2018) presented a new analysis of fine timescales revealing a two-component structure: a short hard spike followed by a longer soft tail. The total duration of the prompt episode shown as a two-component structure was 0.08 ± 0.93 s, and the fluence was $(1.2 \pm 0.1) \times 10^{-7}$ erg cm $^{-2}$ for the main peak and $(2.0 \pm 0.2) \times 10^{-8}$ erg cm $^{-2}$ for the soft tail. The Chandra X-ray Observatory ACIS-S reported two observations, 7.94 and 39.68 days after the BAT trigger, with durations of ~ 4.1 hr each (Fong et al. 2016). Optical/near-IR observations and upper limits were collected with Magellan/Baade using IMACS with the *r*, *g*, *i*, and *z* optical bands; the Very Large Telescope equipped with the High Acuity Wide-field K-band Imager I with the *J*, *H*, *K*, and *Y* optical bands (Fong 2015; Levan et al. 2015); TNG using NICS with the *J* optical band (D’Avanzo et al. 2015); Gemini-S instrumented with GMOS (*r* band; Fong et al. 2015); the United Kingdom Infrared Telescope with the instrument WFCAM (*J* and *K* bands); and HST using the WFC3 with the F160W and F606W bands (Fong et al. 2016). Spectroscopic observations in the wavelength range 530–850 nm of 2MASX J12320498–1056010 revealed several prominent absorption features that could associate GRB 150101B with an early-type host galaxy located at $z = 0.1343 \pm 0.0030$ (Levan et al. 2015; Fong et al. 2016).

GRB 160821B—The Swift-BAT and Fermi-GBM triggered and located GRB 160821B at 22:29:13 and 22:29:13.33 UT on 2016 August 21, respectively (Siegel et al. 2016; Stanbro & Meegan 2016). The Swift-BAT light curve in the energy range of 15–150 keV exhibited a single peak with a duration and total fluence of 0.48 ± 0.07 s and $(1.1 \pm 0.1) \times 10^{-7}$ erg cm $^{-2}$, respectively (Palmer et al. 2016). The Fermi-GBM light curve in the energy range of 8–1000 keV showed a single peak (similar to the Swift-BAT profile) with a duration and total fluence of ~ 1.2 s and $(2.52 \pm 0.19) \times 10^{-6}$ erg cm $^{-2}$, respectively (Lü et al. 2017). They estimated that the isotropic energy released in gamma rays was $E_{\text{iso}} = (2.1 \pm 0.2) \times 10^{50}$ erg. Swift-XRT started detecting photons 57 s after the trigger time (Siegel et al. 2016). Swift-UVOT began observing the field of GRB 160821B 76 s after the Swift-BAT trigger. Although no photons in the optical band were detected during the first hours, constraining upper limits were placed (Evans et al. 2016). The William Herschel Telescope on La Palma detected diverse emission lines in the visible (including H β , [O III] 4959/5007, and H α), locating this burst with a redshift of $z = 0.16$ (Levan et al. 2016).

SN 2020bvc—On 2020 February 4 at 14:52:48 UTC, SN 2020bvc was first detected by the ASAS-SN Brutus instrument using the *g* Sloan filter with a reported location of R.A. = $14^{\text{h}}33^{\text{m}}57^{\text{s}}.024$, decl. = $+40^{\circ}14'36''85$ (J2000). It was associated with the host galaxy UGC 09379, with a redshift of $z = 0.025235$ (Stanek 2020). A later report confirmed this association and redshift and, based on the blue featureless continuum and the absolute magnitude at discovery of -18.1 , classified this event as a young CC SN (Hiramatsu et al. 2020).

A later analysis (Perley et al. 2020) of the spectrum obtained with the SPRAT spectrograph on the 2 m robotic Liverpool Telescope showed excellent agreement with the GRB-associated broad-line SN Ic 1998bw; thus, it was categorized as a young broad-line Ic SN. It was noticed to have an extremely fast rise by a steep decay in the 2 days following the first detection. It was later shown to rise toward a second peak. The decay temporal index reported by Izzo et al. (2020) was $\alpha_{\text{dec}} = 1.35 \pm 0.9$. Twelve days later, on February 16, the VLA observed the position of SN 2020bvc and detected a point source with a flux density of $66 \mu\text{Jy}$ in the X band and a luminosity of 1.3×10^{27} erg s $^{-1}$ Hz $^{-1}$ (Ho 2020). On the same day, a 10 ks Chandra observation was obtained. The data were reduced and the spectrum fitted with a power-law source model with a flux of approximately 10^{-14} erg cm $^{-2}$ s $^{-1}$ (Ho et al. 2020a).

3.2. Analysis and Discussion

GRB 080503—We apply the Bayesian statistical approach of Markov Chain Monte Carlo (MCMC) simulations to determine the best-fit values of the parameters that characterize the multiwavelength afterglow observations with their upper limits (e.g., see Fraija et al. 2019c). A set of eight parameters, $\{E, n, p, \epsilon_{\text{B}}, \Gamma, \epsilon_e, \theta_j, \text{ and } \theta_{\text{obs}}\}$, is required by our synchrotron afterglow model evolving in a constant-density medium to describe the multiwavelength observations. A total of 17,300 samples and 4100 tuning steps is used to describe the entire data set. Normal distributions are used to characterize all of the parameters. Corner plots illustrate the best-fit values and the median of the posterior distributions of the parameters, as shown in Figure 4. In this figure, the best-fit values are highlighted in green, and the medians of the posterior distributions are presented in Table 5.

The multiwavelength afterglow observations, together with the fits computed using the synchrotron off-axis model evolving in a constant-density medium, are shown in Figure 5. The synchrotron light curves obtained with the same electron population and displayed in the optical (*R* and *g*) and X-ray bands support the scenario of one emitting zone inside an off-axis outflow. The fact that the beaming cone of synchrotron radiation reaches our line of sight is compatible with the best-fit value of the viewing angle $\theta_{\text{obs}} = 15.412_{-0.269}^{+0.268}$ $^{\circ}$ and the rebrightening in all bands at ~ 1 day. The best-fit value of the electron spectral index $p = 2.319_{-0.049}^{+0.049}$ matches the typical value observed when forward-shocked electrons radiate by synchrotron emission (see, e.g., Kumar & Zhang 2015). It confirms that these multiwavelength observations originate during the afterglow.

The best-fit value of the constant-density medium $n = 4.221_{-0.103}^{+0.102} \times 10^{-2}$ cm $^{-3}$ indicates that GRB 080503 took place in a medium with very low density comparable to an intergalactic density environment with $\sim 10^{-3}$ cm $^{-3}$. The best-fit values of the bulk Lorentz factor ($\Gamma = 2.939_{-0.078}^{+0.101} \times 10^2$) and the equivalent kinetic energy ($E = 2.156_{-0.295}^{+0.294} \times 10^{52}$ erg) indicate that synchrotron radiation is emitted from a narrowly collimated outflow.

Perley et al. (2009) analyzed the multiwavelength observations at ~ 1 day. They dismissed the kilonova-like emission proposed by Li & Paczyński (1998) and gave an afterglow explanation, pointing out that the X-ray and optical data had similar evolutions. They hypothesized that the late optical and X-ray bumps might be explained in a slightly off-axis jet or a refreshed shock. The faint afterglow compared to the intense prompt emission could be described in the very low circumburst medium. Gao et al. (2015) claimed that under certain requirements on the bulk Lorentz factor

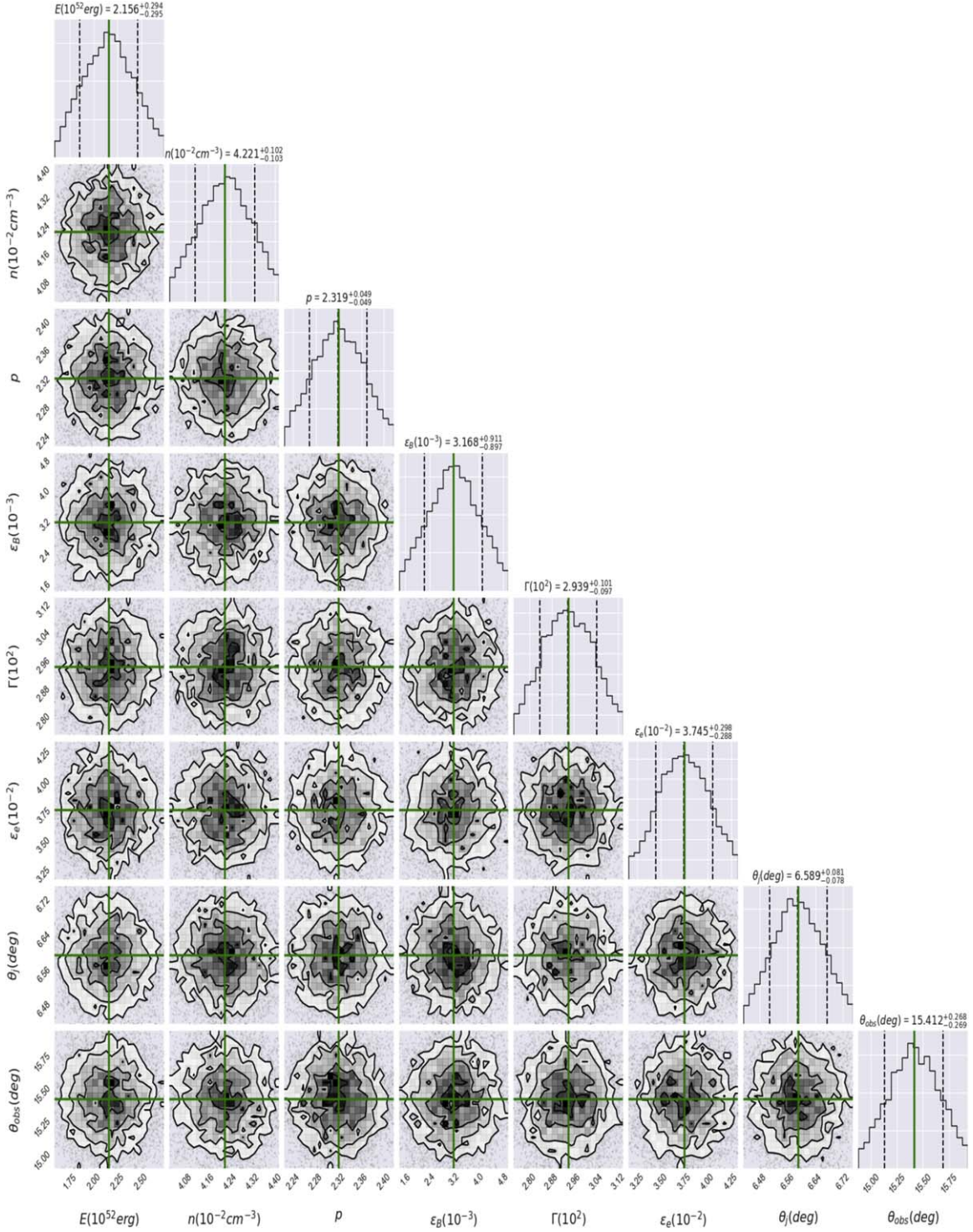


Figure 4. Corner plot of the parameters derived from fitting the multiwavelength light curves of GRB 080503 with a synchrotron off-axis model, together with median values (green lines) and 1σ credible intervals (dashed lines). The MCMC summary statistics for all parameters are listed in Table 5. A set of normal distributions is made for the priors.

and the beaming angle of the relativistic jet, refreshed shocks in the synchrotron forward- and reverse-shock scenarios could adequately describe the late rebrightening in GRB 080503. Finally, Gao et al. (2015) proposed that the late optical peak was due to the emission from a magnetar-powered “merger-nova,” and the X-ray hump from magnetic dissipation of the magnetar dipole spin-down luminosity. According to our analysis, these observations at ~ 1 day are consistent with the afterglow emission found

off-axis. It is worth noting that measurements of the linear polarization of the optical emission could discriminate between an on- and off-axis scenario, and GWs would provide information about the progenitor (a merger of NS–NS or BH–NS or a stable NS).

GRB 140903A—We once again conducted MCMC simulations with a set of eight parameters, $\{E, n, p, \epsilon_B, \Gamma, \epsilon_e, \theta_j, \text{ and } \theta_{\text{obs}}\}$, to find the best-fit values that describe the

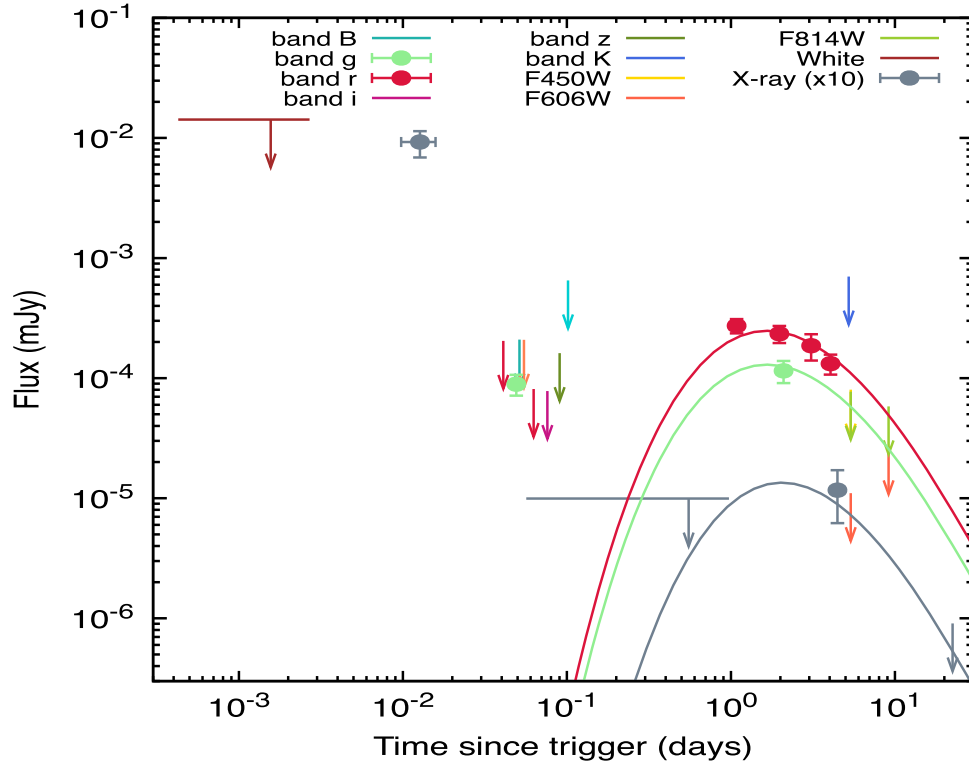


Figure 5. The X-ray and optical light curves of GRB 080503 with the best-fit curve of synchrotron afterglow model. The synchrotron light curves are shown at 1 keV (gray), the R band (red), and the g band (green). Data points are taken from Perley et al. (2009).

Table 4
Evolution of the Density Parameter $F_\nu \propto A_k^{\alpha_k}$ in Each Cooling Condition of the Synchrotron Afterglow Model

	Coasting Phase		Deceleration Phase (Off-axis Afterglow)		Deceleration Phase (On-axis Afterglow)		Post-Jet Break Phase	
	β	α_k	α_k	α_k	α_k	α_k	α_k	α_k
$\nu_{a,3} < \nu_c < \nu_m$								
$\nu < \nu_{a,3}$	-2	-1	0	$\frac{4}{4-k}$	$-\frac{3}{3-k}$			
$\nu_{a,3} < \nu < \nu_c$	$-\frac{1}{3}$	2	$\frac{8}{3}$	$\frac{10}{3(4-k)}$	$\frac{4}{4-k}$			
$\nu_c < \nu < \nu_m$	$\frac{1}{2}$	$\frac{3}{4}$	$\frac{9}{4}$	0	$-\frac{3}{3-k}$			
$\nu_m < \nu$	$\frac{p}{2}$	$\frac{p+2}{4}$	$\frac{10-p}{4}$	0	$-\frac{4(3-k)}{4(3-k)}$			
$\nu_{a,1} < \nu_m < \nu_c$								
$\nu < \nu_{a,1}$	-2	0	0	$-\frac{2}{4-k}$	$-\frac{2}{3-k}$			
$\nu_{a,1} < \nu < \nu_m$	$-\frac{1}{3}$	$\frac{4}{3}$	$\frac{8}{3}$	$\frac{2}{4-k}$	$\frac{3(3-k)}{3(3-k)}$			
$\nu_m < \nu < \nu_c$	$\frac{p-1}{2}$	$\frac{p+5}{4}$	$\frac{11-p}{4}$	$\frac{2}{4-k}$	$\frac{3-p}{4(3-k)}$			
$\nu_c < \nu$	$\frac{p}{2}$	$\frac{p+2}{4}$	$\frac{10-p}{4}$	0	$-\frac{p+2}{4(3-k)}$			
$\nu_m < \nu_{a,2} < \nu_c$								
$\nu < \nu_m$	-2	0	0	$-\frac{2}{4-k}$	$-\frac{2}{3-k}$			
$\nu_m < \nu < \nu_{a,2}$	$-\frac{5}{2}$	$-\frac{1}{4}$	$\frac{1}{4}$	$-\frac{2}{4-k}$	$-\frac{7}{4(3-k)}$			
$\nu_{a,2} < \nu < \nu_c$	$\frac{p-1}{2}$	$\frac{p+5}{4}$	$\frac{11-p}{4}$	$\frac{2}{4-k}$	$\frac{3-p}{4(3-k)}$			
$\nu_c < \nu$	$\frac{p}{2}$	$\frac{p+2}{4}$	$\frac{10-p}{4}$	0	$-\frac{p+2}{4(3-k)}$			

multiwavelength afterglow observations with their upper limits. A set of eight parameters, $\{E, n, p, \varepsilon_B, \Gamma, \varepsilon_e, \theta_j, \text{ and } \theta_{\text{obs}}\}$, is required. To represent the entire observation in this scenario, a total of 16,200 samples and 4150 tuning steps were used. Figure 6 displays the best-fit values in green and the median of

the posterior distributions of the parameters. In Table 5, the best-fit values are shown and the median of the posterior distributions is presented.

The multiwavelength observations of GRB 140903A are shown in Figure 7, together with the fits derived using the

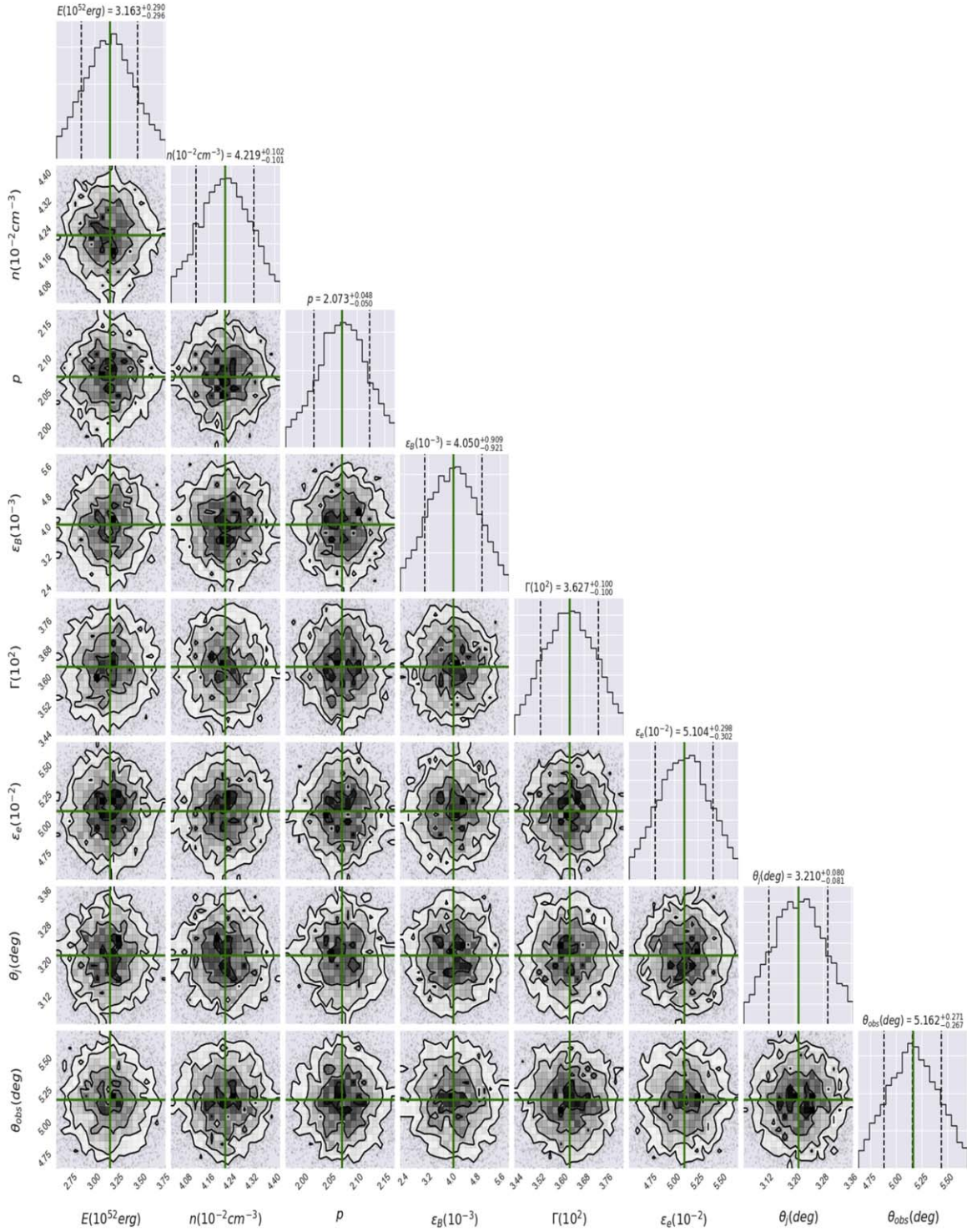


Figure 6. Same as Figure 4 but for GRB 140903A.

synchrotron off-axis model evolving in a homogenous density. The best-fit values of the viewing angle $\theta_{\text{obs}} = 5.162^{+0.271}_{-0.267} \text{ }^\circ$ and the half-opening angle $\theta_j = 3.210^{+0.080}_{-0.081} \text{ }^\circ$ indicate that the relativistic outflow was slightly off-axis. The best-fit value of the constant-density medium $n = 4.219^{+0.102}_{-0.101} \times 10^{-2} \text{ cm}^{-3}$ indicates that GRB 140903A took place in a medium with very low density comparable to an intergalactic density environment. The best-fit values of the bulk Lorentz factor ($\Gamma = 3.627^{+0.100}_{-0.100} \times 10^2$) and the equivalent kinetic energies ($E =$

$3.163^{+0.290}_{-0.296} \times 10^{52} \text{ erg}$) indicate that synchrotron emission is radiated from a narrowly collimated jet. The best-fit values of the microphysical parameters $\epsilon_e = 5.104^{+0.298}_{-0.302} \times 10^{-2}$ and $\epsilon_B = 4.050^{+0.909}_{-0.921} \times 10^{-3}$ and the spectral index of the shocked electrons $2.073^{+0.048}_{-0.050}$ are similar to those reported in Troja et al. (2016). This spectral index is in the typical range of those accelerated in forward shocks (see, e.g., Kumar & Zhang 2015), thus reaffirming the afterglow as its origin. Troja et al. (2016) reported and analyzed the afterglow observations of GRB

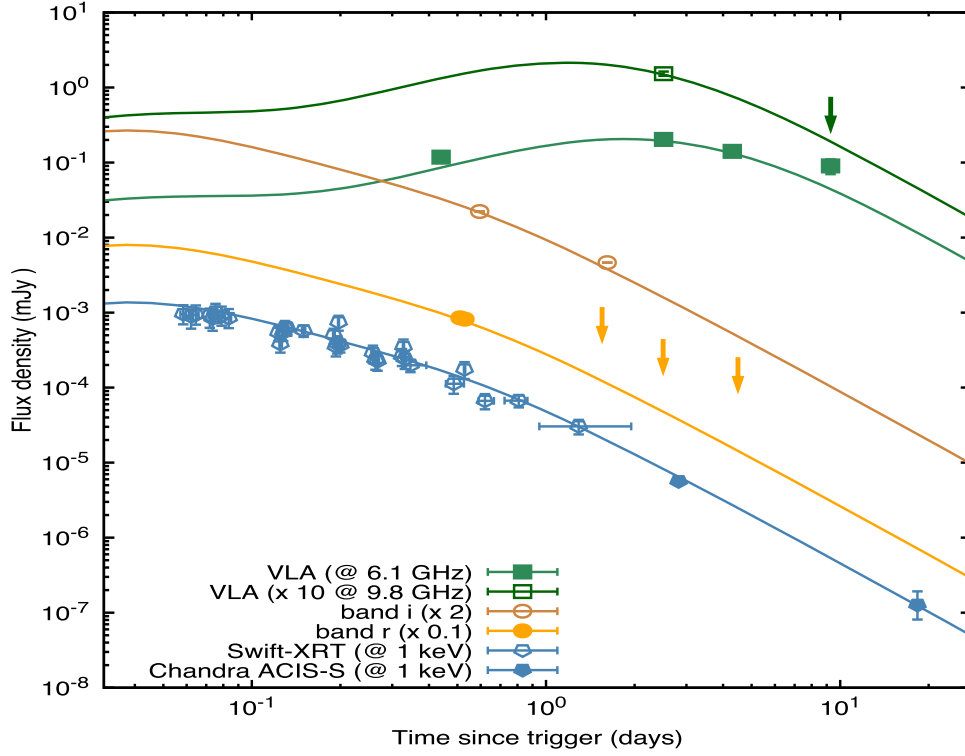


Figure 7. The X-ray, optical, and radio light curves of GRB 140903A with the best-fit curve of the synchrotron afterglow model. The synchrotron light curves are shown at 1 keV (blue), R band (gold), i band (brown), 9.8 GHz (dark green), and 6.1 GHz (light green). Data points are taken from Troja et al. 2016.

Table 5
Median Values of Parameters Used to Describe the Multiwavelength Afterglow Observations of a Sample of sGRBs and IGRBs

Parameters	GRB 080503	GRB 140903A	GRB 150101B	GRB 160821B	SN 2020bvc
E (10^{52} erg)	$2.156^{+0.294}_{-0.295}$	$3.163^{+0.290}_{-0.296}$	$1.046^{+0.120}_{-0.124}$	$0.118^{+0.021}_{-0.021}$	$0.238^{+0.011}_{-0.010}$
n (10^{-2} cm^{-3})	$4.221^{+0.102}_{-0.103}$	$4.219^{+0.102}_{-0.101}$	$0.164^{+0.021}_{-0.021}$	$0.869^{+0.093}_{-0.090}$...
$^a A_w$ (10^{-13} $\text{cm}^{1/2}$)	$3.340^{+0.195}_{-0.193}$
p	$2.319^{+0.049}_{-0.049}$	$2.073^{+0.048}_{-0.050}$	$2.150^{+0.217}_{-0.215}$	$2.220^{+0.021}_{-0.021}$	$2.313^{+0.037}_{-0.035}$
ϵ_B (10^{-3})	$3.168^{+0.911}_{-0.897}$	$4.050^{+0.909}_{-0.921}$	$0.147^{+0.124}_{-0.094}$	$0.559^{+0.437}_{-0.365}$	$5.623^{+0.020}_{-0.020}$
ϵ_e (10^{-2})	$3.745^{+0.298}_{-0.288}$	$5.104^{+0.298}_{-0.302}$	$1.001^{+0.176}_{-0.164}$	$0.155^{+0.021}_{-0.021}$	$38.951^{+0.295}_{-0.288}$
Γ (10^2)	$2.939^{+0.101}_{-0.097}$	$3.627^{+0.100}_{-0.100}$	$4.251^{+0.468}_{-0.453}$	$4.559^{+0.361}_{-0.358}$	$2.291^{+0.100}_{-0.100}$
θ_j ($^\circ$)	$6.589^{+0.081}_{-0.078}$	$3.210^{+0.080}_{-0.081}$	$6.887^{+0.662}_{-0.682}$	$8.002^{+0.817}_{-0.809}$	$2.121^{+0.078}_{-0.079}$
θ_{obs} ($^\circ$)	$15.412^{+0.268}_{-0.269}$	$5.162^{+0.271}_{-0.267}$	$14.114^{+2.327}_{-2.179}$	$10.299^{+1.125}_{-1.135}$	$12.498^{+0.268}_{-0.281}$

Note.

^a This value is used when $k = 1.5$.

140903A for the first 2 weeks. Applying the fireball scenario, they demonstrated that this burst was caused by a collimated jet seen off-axis and also connected with a compact binary object. The X-ray “plateau” seen in GRB 140903A was attributed to the energy injection into the decelerating blast wave by Zhang et al. (2017). The authors then modeled the late afterglow emission, which required a half-opening angle of $\approx 3^\circ$, similar to the value found with our model. Object GRB 140903A was formed in a collimated outflow observed off-axis that decelerates in a uniform density, according to our findings.

GRB 150101B—We use MCMC simulations with the eight parameters used for GRB 080503 and GRB 140903A to find the best-fit values that model the X-ray afterglow observations with the optical upper limits. To represent all of the data in this case, a total of 15,900 samples and 4400 tuning steps are used.

Figure 8 displays the best-fit values and the median of the posterior distributions of the parameters. In Table 5, the best-fit values are shown and the median of the posterior distributions is presented.

The X-ray, optical, and radio observations and upper limits, as well as the fit obtained using the synchrotron off-axis model evolving in homogeneous density, are shown in Figure 9. The left panel shows the light curves at 1 keV (gray), the R band (blue), the F606W filter (orange), and the F160W filter (green), and the right panel displays the broadband spectral energy distributions (SEDs) at 2 (red) and 9 (green) days. The red shaded region corresponds to the spectrum of AT 2017gfo, which is adapted by Troja et al. (2018). The best-fit values of the viewing angle $\theta_{\text{obs}} = 14.114^{+2.327}_{-2.179}^\circ$ and the half-opening angle $\theta_j = 6.887^{+0.662}_{-0.682}^\circ$ can explain the lack of X-ray emission

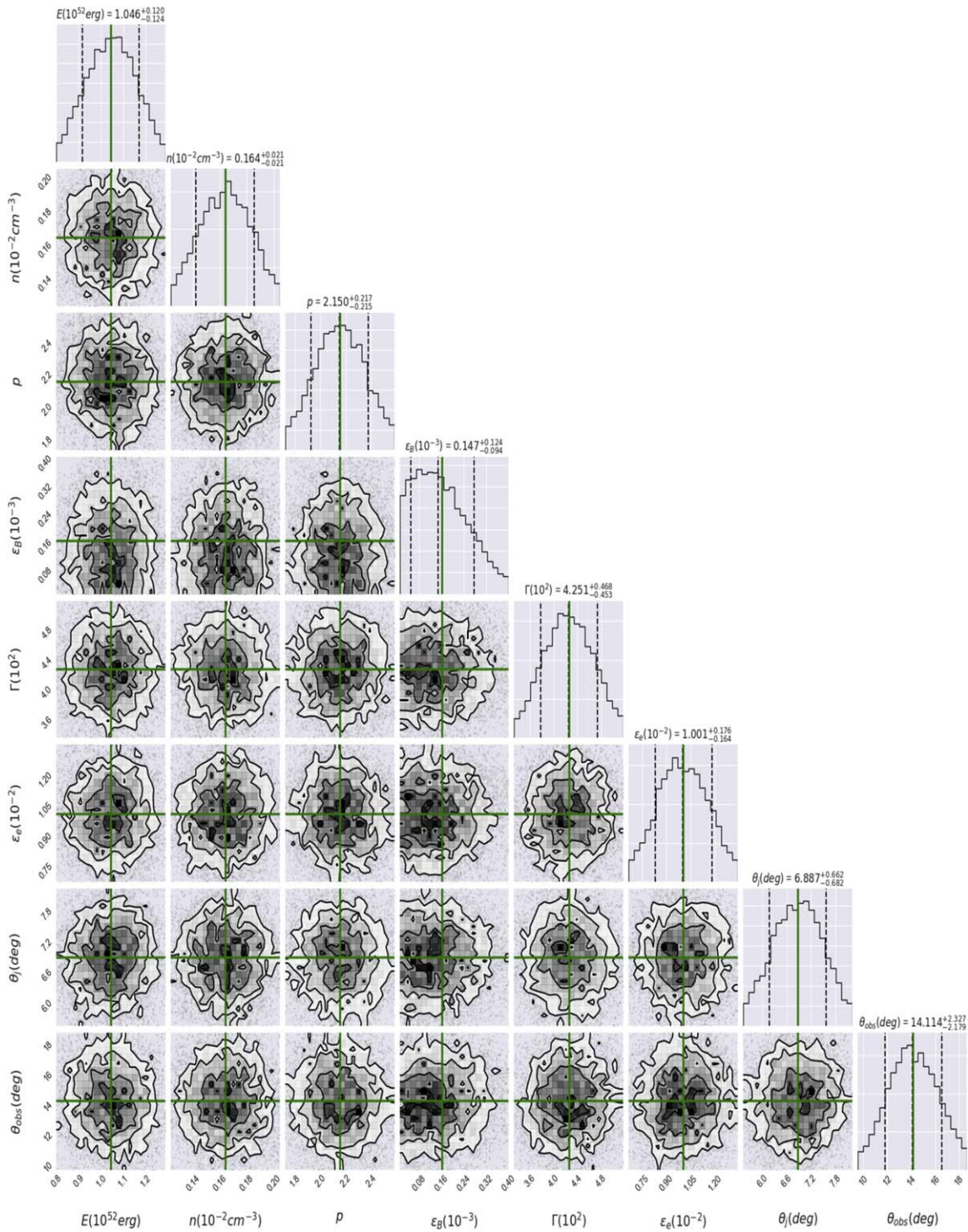


Figure 8. Same as Figure 4 but for GRB 150101B.

during the first day. The best-fit value of the constant-density medium $n = 0.164^{+0.021}_{-0.021} \times 10^{-2} \text{ cm}^{-3}$ indicates that GRB 150101B, like other short bursts, happened in an environment with very low density. The best-fit values of the bulk Lorentz factor ($\Gamma = 4.251^{+0.468}_{-0.453} \times 10^2$) and the equivalent kinetic energy ($E = 1.046^{+0.120}_{-0.124} \times 10^{52} \text{ erg}$) suggest that synchrotron afterglow emission is emitted from a narrowly collimated jet. The values of the spectral index of the electron population, the circumburst density, the microphysical parameters, and the viewing angle disfavor the isotropic cocoon model reported in

Troja et al. (2018) and are consistent with the values of an outflow when homogeneous density is taken into account. The best-fit values of the spectral index of the shocked electrons $2.150^{+0.217}_{-0.215}$ are similar to those reported in synchrotron afterglow models (see, e.g., Kumar & Zhang 2015).

GRB 160821B—We require MCMC simulations with eight parameters used in the previous bursts to find the best-fit values that describe the multiwavelength afterglow observations with their upper limits. To characterize the complete data in this scenario, a total of 17,300 samples and 7400 tuning steps are

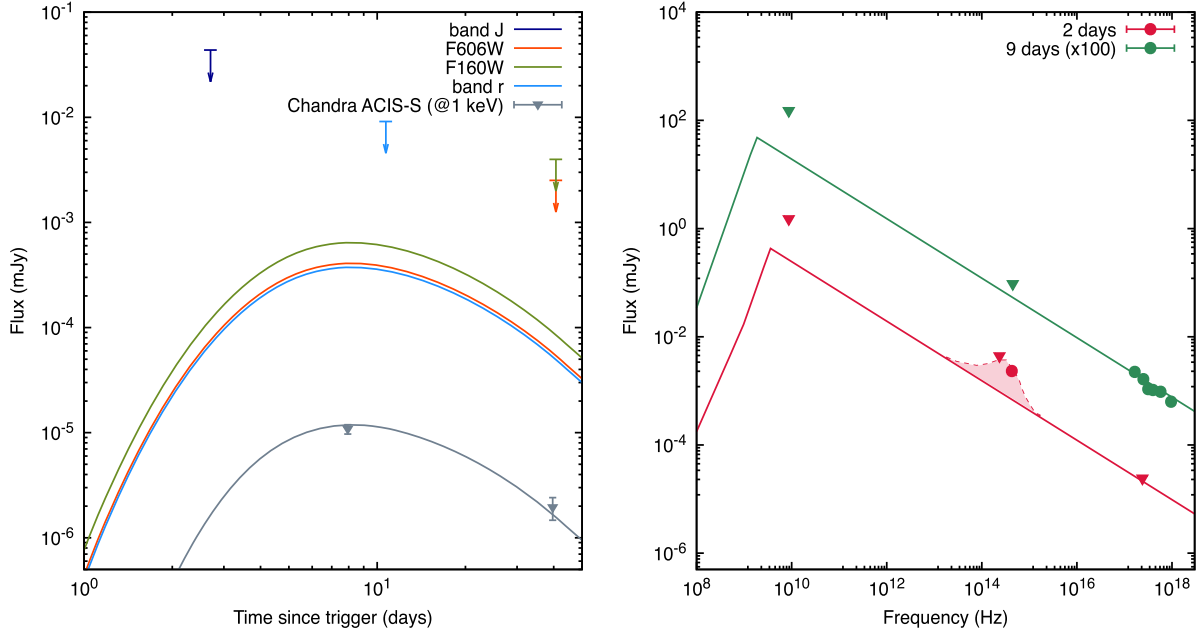


Figure 9. Left: X-ray light curves with the optical upper limits of GRB 150101B with the best-fit curve of the synchrotron afterglow model. The synchrotron light curves are shown at 1 keV (gray), the *R* band (blue), the F606W filter (orange), and the F160W filter (green). Data points are taken from Fong et al. (2016) and Troja et al. (2018). Right: broadband SEDs of the X-ray, optical, and radio afterglow observations and upper limits with the best-fit synchrotron curves (lines) at 2 (red) and 9 (green) days. The red shaded region corresponds to the spectrum of AT 2017gfo, which is adapted by Troja et al. 2018.

used. Figure 10 exhibits the best-fit values and the median of the posterior distributions of the parameters. In Table 5, the best-fit values and the medians of the posterior distributions are presented.

The multiwavelength observations since 0.2 days after the GBM trigger are shown in Figure 11, together with the fits found requiring the synchrotron off-axis model evolving in a homogeneous density. The left panel exhibits the light curves at 1 keV (gray), the *z* band (purple), the F606W filter (dark red), the *R* band (salmon), the F110W filter (cyan), the F160W filter (light blue), the *K_s* band (dark blue), the X-channel (olive), and the C-channel (emerald green), and the right panel shows the broadband SEDs of the X-ray, optical, and radio afterglow observations at 2 hr (red), 2 days (blue), and 4 days (green). The shaded areas in blue and green correspond to blackbody spectra with decreasing temperatures first suggested in Jin et al. (2018) and then confirmed by Lamb et al. (2019) and Troja et al. (2019a). The kilonova emission is the most natural explanation for the “new” radiation component. The Swift-XRT-UVOT data were received from the public database from the official Swift website.¹² The *C* band displays radio data; the white, *v*, *b*, *u*, UVW1, UVW2, and UVM2 bands display Swift-UVOT data; and the 1 keV band displays XRT data. Using the conversion factor proposed in Evans et al. (2010), the flux density of the XRT data is extrapolated from 10 to 1 keV. The best-fit values of circumburst density $n = 0.869_{-0.090}^{+0.093} \times 10^{-2} \text{ cm}^{-3}$, the spectral index of shocked electrons $p = 2.220_{-0.021}^{+0.021}$, the viewing angle $\theta_{\text{obs}} = 10.299_{-1.135}^{+1.125} \text{ }^\circ$, and the half-opening angle $\theta_j = 8.002_{-0.809}^{+0.817} \text{ }^\circ$ are similar to those previously reported in Troja et al. (2019b). The best-fit values of the viewing angle $\theta_{\text{obs}} = 10.299_{-1.135}^{+1.125} \text{ }^\circ$ and the half-opening angle $\theta_j = 8.002_{-0.809}^{+0.817} \text{ }^\circ$ suggest that the relativistic outflow was slightly off-axis. The best-fit values of the bulk Lorentz

factor ($\Gamma = 4.559_{-0.358}^{+0.361} \times 10^2$) and the equivalent kinetic energy ($E = 0.118_{-0.021}^{+0.021} \times 10^{52} \text{ erg}$) indicate that synchrotron afterglow emission is emitted from a narrowly collimated jet.

SN 2020bvc—We use MCMC simulations to find the best-fit values of the parameters that describe the X-ray afterglow observations. A set of eight parameters, $\{E, A_w, p, \varepsilon_B, \Gamma, \varepsilon_e, \theta_j, \text{ and } \theta_{\text{obs}}\}$, is used to describe the X-ray observations. To characterize the complete data in this scenario, a total of 17,100 samples and 7200 tuning steps are used. Figure 12 exhibits the best-fit values and the median of the posterior distributions of the parameters. In Table 5, the best-fit values and the medians of the posterior distributions are presented. We assumed a stratified medium with a parameter $k = 1.5$, consistent with the proposal by Izzo et al. (2020). Our best-fit values, however, are slightly different. We propose that the emission is due to an off-axis jet that is \approx five times more energetic and with half of the off-axis angle compared to the values of Izzo et al. (2020). This discrepancy is due to a different choice of the electron velocity distribution index p , as our MCMC simulation suggested $p = 2.313_{-0.035}^{+0.037}$, in contrast with the value of $p = 2$ used by the cited authors. Figure 13 shows the X-ray observations of SN 2020bvc with the best-fit synchrotron light curve generated by the deceleration of an off-axis jet in a medium with stratification parameter $k = 1.5$.

Our results are consistent with the X-ray observations before and after ~ 4 days since the trigger time, when the observed flux increases and decreases, respectively. Initially, the flux increases with a minimum rise index of $\alpha_{\text{m, ris}} > 1.65$; later, the observed flux decreases with $\alpha_{\text{dec}} = -1.35 \pm 0.09$ (Izzo et al. 2020). The allowed value of the minimum rise index is estimated considering a simple power-law function, the X-ray upper limit, and the maximum flux. For instance, given the best-fit value of $p = 2.313_{-0.035}^{+0.037}$ and for $0 < k < 1.5$, the temporal rise and decay indexes are $1.65 \pm 0.03 \leq \alpha_{\text{ris}} \leq 4.53 \pm 0.03$ and $\alpha_{\text{dec}} = -1.24 \pm 0.03$, respectively, for $\nu_c < \nu$

¹² <https://swift.gsfc.nasa.gov/cgi-bin/sdc/ql?>

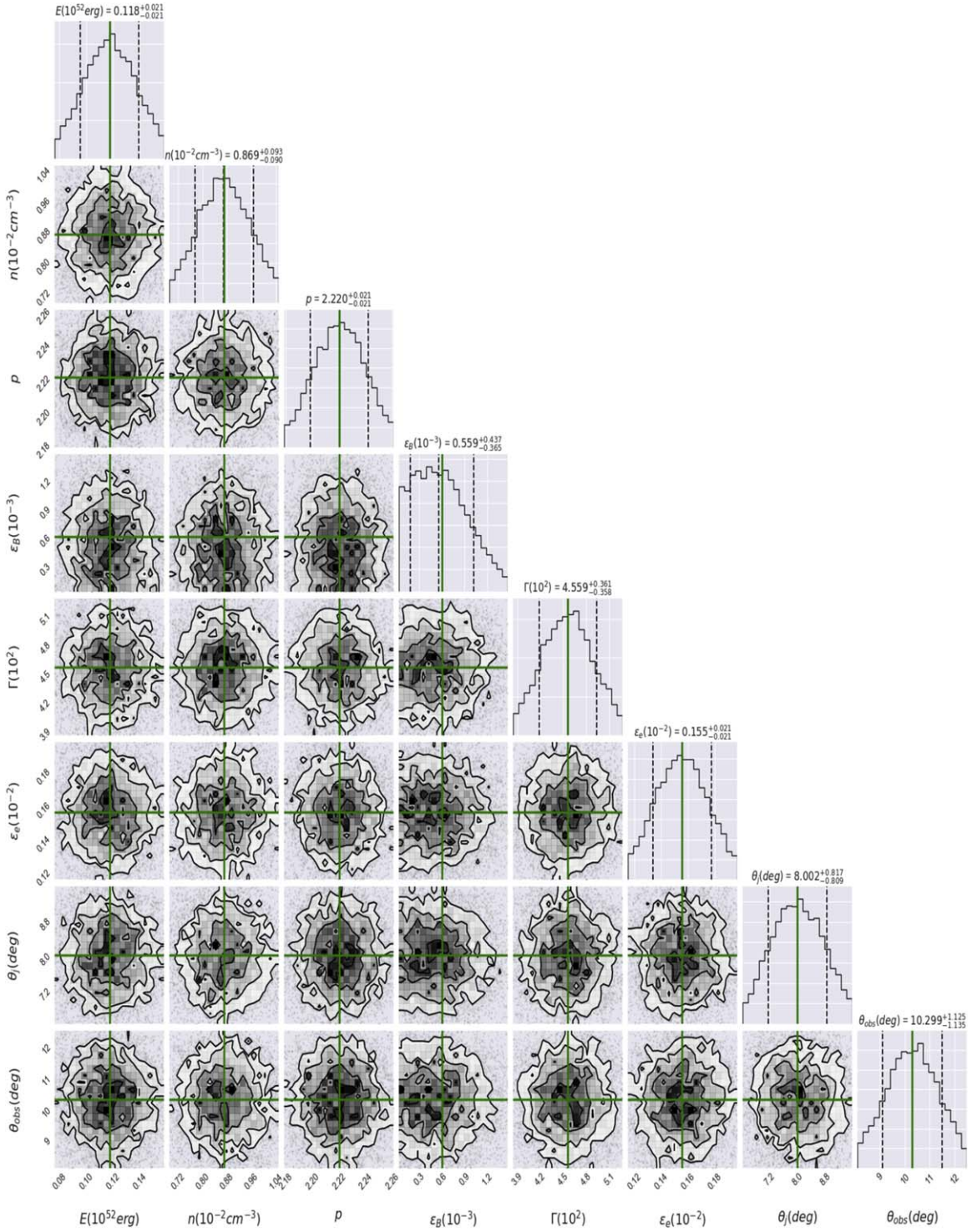


Figure 10. Same as Figure 4 but for GRB 160821B.

(see Table 1). For $k > 1.5$, the expected rise index would be $\alpha_{\text{ris}} < 1.65$, which cannot reproduce the X-ray observations.

The synchrotron scenario from on-axis outflow in a very low density environment is disfavored for $p \sim 2$. The closure relations of the synchrotron on-axis model from an outflow decelerating in a stratified environment for k in general can be estimated. During the coasting and deceleration phases, the bulk Lorentz factor evolves as $\Gamma \propto t^0$ and $\Gamma \propto t^{\frac{k-3}{8-2k}}$, respectively. Therefore, the synchrotron flux during the slow-cooling regime evolves as $F_\nu \propto$

$t^{\frac{12-k(p+5)}{4}} \nu^{-\frac{p-1}{2}}$ for $\nu_m < \nu < \nu_c$ and $\propto t^{\frac{8-k(p+2)}{4}} \nu^{-\frac{p}{2}}$ for $\nu_c < \nu$ during the coasting phase and $F_\nu \propto t^{-\frac{12(p-1)+k(5-3p)}{4(4-k)}} \nu^{-\frac{p-1}{2}}$ for $\nu_m < \nu < \nu_c$ and $\propto t^{-\frac{3p-2}{4}} \nu^{-\frac{p}{2}}$ for $\nu_c < \nu$ during the deceleration phase. It is worth noting that for the cooling condition $\nu_c < \nu$ and with a value of $p = 2.5$, the temporal evolution is only consistent for $k \lesssim 0.3$

The best-fit values of the bulk Lorentz factor ($\Gamma = 2.291^{+0.100}_{-0.100} \times 10^2$), the equivalent kinetic energy ($E = 2.38^{+0.01}_{-0.01} \times 10^{51}$ erg), and the half-opening angle $\theta_j = 2.121^{+0.078}_{-0.079}^\circ$ indicate that synchrotron

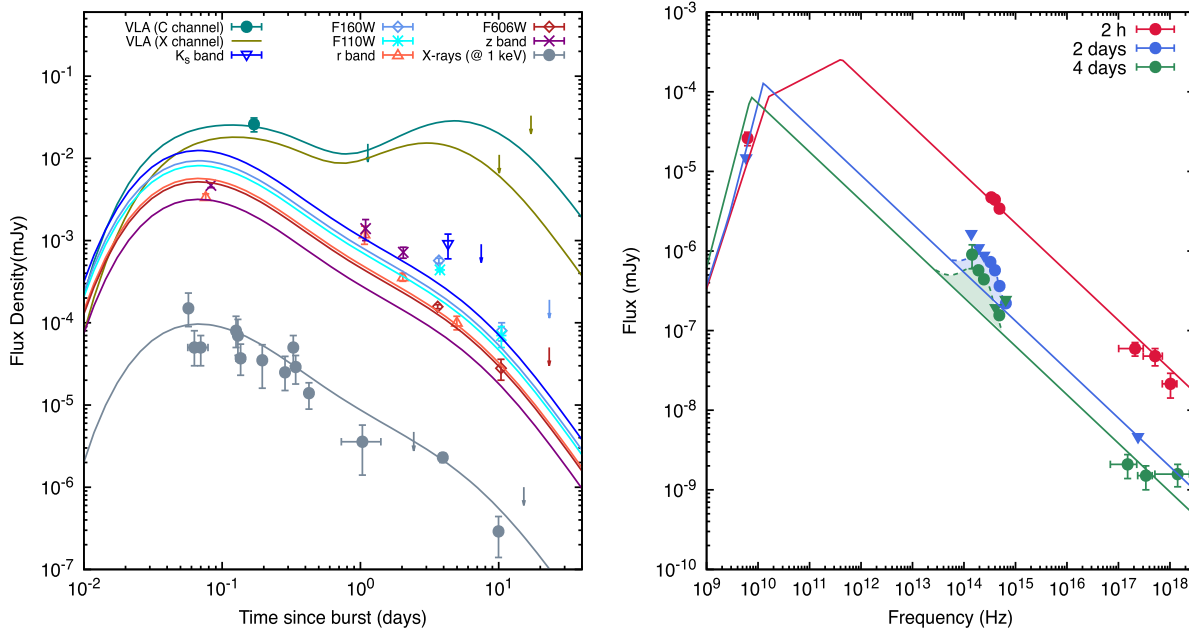


Figure 11. Left: X-ray, optical, and radio light curves of GRB 160821B with the best-fit curve of the synchrotron afterglow model. The synchrotron light curves are shown at 1 keV (gray), the z band (purple), the F606W filter (dark red), the R band (salmon), the F110W filter (cyan), the F160W filter (light blue), the K_s band (dark blue), the X-channel (olive), and the C-channel (emerald green). Data points are taken from Troja et al. (2019a). Right: broadband SEDs of the X-ray, optical, and radio afterglow observations with the best-fit synchrotron curves (lines) at 2 hr (red), 2 days (blue), and 4 days (green). The shaded areas correspond to blackbody spectra with decreasing temperatures from Troja et al. (2019a).

emission is produced from a narrowly collimated outflow decelerating in an external medium. The best-fit values of the viewing angle $\theta_{\text{obs}} = 12.498^{+0.268}_{-0.281}$ ° and the half-opening angle $\theta_j = 2.121^{+0.078}_{-0.079}$ ° are consistent with the lack of early multi-wavelength observations.

Lü et al. (2012) discovered a correlation between the bulk Lorentz factors and the isotropic gamma-ray luminosities in a sample of GRBs. Fan et al. (2012) showed that the correlations of these parameters were consistent with the parameters predicted in the photospheric emission model. Figure 14 shows the diagram of the bulk Lorentz factors and the isotropic gamma-ray luminosities of sGRBs described in this work (red) with those (gray) reported in Lü et al. (2012). For off-axis sGRBs, we found an empirical correlation $\Gamma = a(L/10^{52} \text{ erg})^b$ with $a = (3.27 \pm 0.39) \times 10^2$ and $b = -(4.9 \pm 2.0) \times 10^{-2}$.

4. Constraints on Possible Afterglow Emission

4.1. The Closest sGRBs Detected by Swift ($100 \text{ Mpc} \leq d_z \leq 200 \text{ Mpc}$)

GRB 050906—Swift-BAT was triggered by GRB 050906 at 10:32:18 UTC on 2005 September 5 with a reported location of R.A. = $03^{\text{h}}31^{\text{m}}13^{\text{s}}$, decl. = $-14^{\circ}37'30''$ (J2000) with a positional accuracy of $3'$ (Krimm et al. 2005). The light curve revealed an excess in the 25–100 keV energy range. The duration and measured fluence in the energy range of 15–150 keV were 128 ± 16 ms and $(5.9 \pm 3.2) \times 10^{-8} \text{ erg cm}^{-2}$, respectively (Parsons et al. 2005). Levan et al. (2008) provided the specifics of Swift’s deep optical and infrared observations. According to the authors, no X-ray or optical/IR afterglow was detected to deep limits, and no residual optical or IR emission was observed.

GRB 070810B—Swift-BAT was triggered by GRB 070810B at 15:19:17 UTC on 2007 August 10 with a reported location of R.A. = $00^{\text{h}}35^{\text{m}}46^{\text{s}}$, decl. = $+08^{\circ}50'07''$ (J2000) with a positional accuracy of $3'$ (Marshall et al. 2007). The

KANATA 1.5 m telescope, the Xinlong TNT 80 cm telescope, the 2 m Faulkes Telescope South, the Shajn 2.6 m telescope, and the Keck I telescope (HST) conducted follow-up observations after the initial detection, which are summarized in Bartos et al. (2019). From the whole observational campaign, only the Shajn telescope detected a source inside the error box of GRB 070810B (Rumyantsev et al. 2007).

GRB 080121—Swift-BAT was triggered by GRB 080121 at 21:29:55 UTC on 2008 January 21 with a reported location of R.A. = $09^{\text{h}}08^{\text{m}}56^{\text{s}}$, decl. = $+41^{\circ}50'29''$ (J2000) and a positional accuracy of $3'$. In the 15–150 keV energy range, the duration and measured fluence were 0.7 ± 0.2 s and $(3 \pm 2) \times 10^{-8} \text{ erg cm}^{-2} \text{ s}^{-1}$, respectively, according to Cummings & Palmer (2008). Follow-up observations were carried out 2.3 days following the burst using the Swift/UVOT and Swift/XRT. Within the Swift-BAT error circle, however, no X-ray afterglow candidate or sources were discovered (Cucchiara & Schady 2008; Troja & Burrows 2008). Within the Swift-BAT error circle, two galaxies were found, indicating a redshift of $z \sim 0.046$ for GRB 080121; however, the isotropic energy released would be several orders of magnitude lower than the usual short-hard bursts (Perley et al. 2008d).

GRB 100216A—Swift-BAT and Fermi-GBM were triggered by GRB 100216A at 10:07:00 UTC on 2010 February 16 with a reported location of R.A. = $10^{\text{h}}17^{\text{m}}03.2^{\text{s}}$, decl. = $+35^{\circ}31'27''.5$ (J2000) with a positional accuracy of $3'$. In the energy range of 15–350 keV, the duration and measured fluence of the single peak were 0.3 s and $(4.7 \pm 3) \times 10^{-8} \text{ erg cm}^{-2}$, respectively (Cummings et al. 2010). The burst was followed up by Swift-XRT and Swift-UVOT from 214.4 to 249.2 ks after the BAT trigger. Within the observation, no fading sources were found, but a source presumed to be 1RXS J101702.9+353404 was discovered within the error circle (Rowlinson et al. 2010; Siegel & Rowlinson 2010).

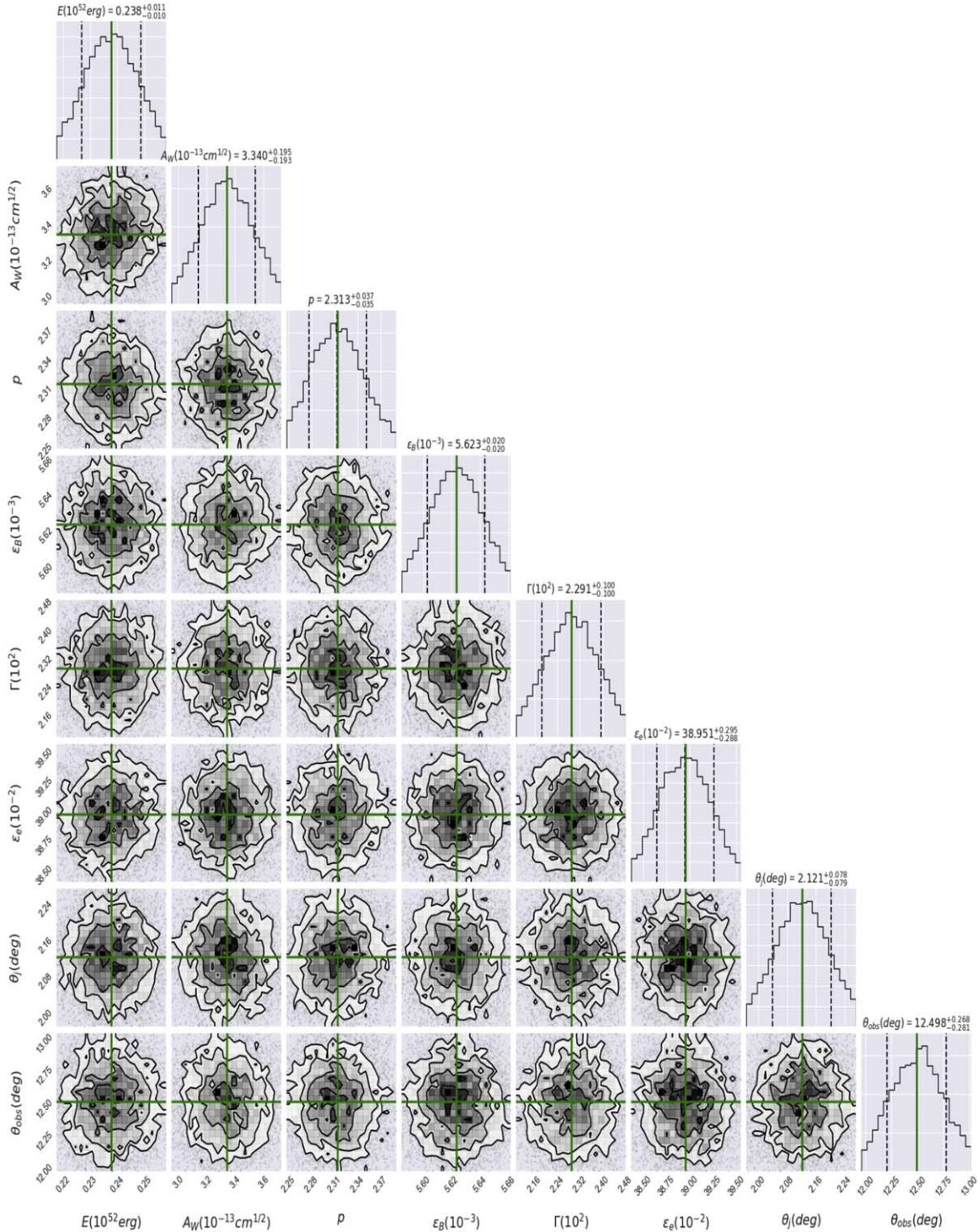


Figure 12. Same as Figure 4 but for SN 2020bvc.

Figure 15 shows the UV and optical upper limits of the closest sGRBs detected by Swift between 100 and 200 Mpc with the synchrotron light curves from an off-axis outflow decelerating in a constant-density medium. The synchrotron light curves are exhibited at the R (black) and UVW1 (gray) bands. The parameter values used to generate the synchrotron light curves are reported in Table 6. We report two values for each parameter; the upper values correspond to synchrotron light

curves in the left panels, and the lower values correspond to the right panels. For the typical values of GRB afterglow reported in Table 6, the synchrotron emission is ruled out for a density of $n = 1 \text{ cm}^{-3}$ but not for $n = 10^{-2} \text{ cm}^{-3}$. The value of the uniform-density medium ruled out in our model is consistent with the mean value reported for sGRBs (e.g., see Berger 2014). It is worth noting that for values of $\epsilon_B < 10^{-4.3}$ and $\epsilon_e < 10^{-1.2}$, the value of the density $n = 1 \text{ cm}^{-3}$ would be allowed.

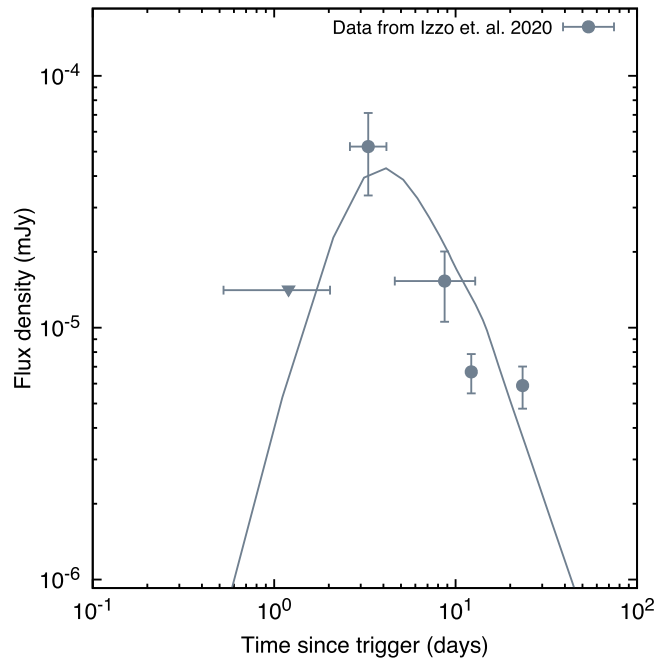


Figure 13. The X-ray data points of SN 2020bvc with the best-fit curve obtained with the model presented in this paper for a stratification parameter of $k = 1.5$. The synchrotron light curve is shown at 1 keV. Data points are taken from Izzo et al. (2020).

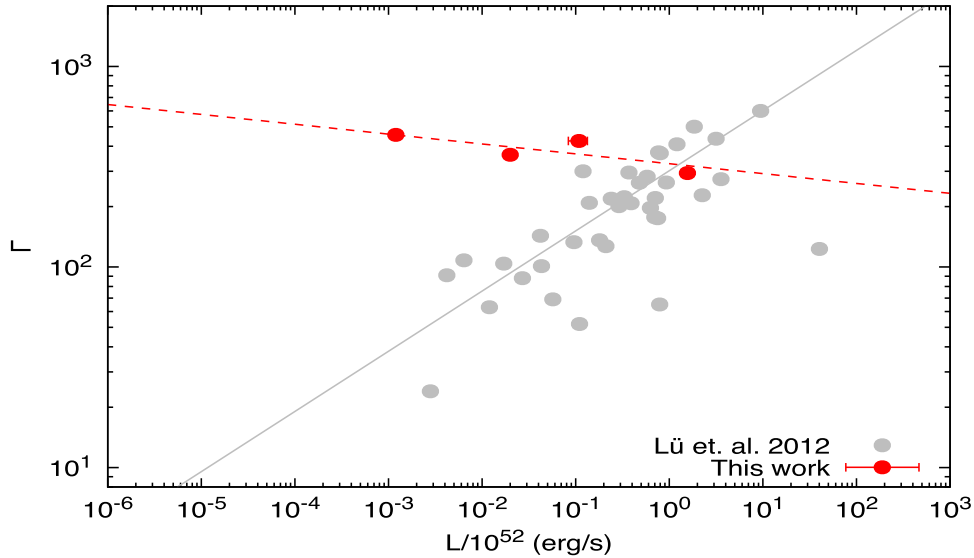


Figure 14. Diagram of bulk Lorentz factors and luminosities for the GRBs discussed in Fan et al. (2012) and Lü et al. (2012) and for sGRBs described in this work. The red dashed line corresponds to the best-fit $\Gamma = a(L/10^{52} \text{ erg/s})^b$ with $a = (3.27 \pm 0.39) \times 10^2$ and $b = -(4.9 \pm 0.20) \times 10^{-2}$.

4.2. Promising GW Events in the Third Observing Run that Could Generate Electromagnetic Emission

Advanced LIGO and Advanced Virgo produced 56 nonretracted alerts of GW candidates during the third observing run (O3), covering almost 1 yr of operations (from 2019 April 1 to 2020 March 27). Nevertheless, three of them have a probability larger than 50% of being terrestrial. The O3 was divided into two epochs associated with “O3a” (from April 1 to September 30) and “O3b” (from November 1 to 2020 March 27). The GW events in

O3a and O3b are listed in the Gravitational Wave Transient Catalog 2 (GWTC-2; Abbott et al. 2021) and Catalog 3 (GWTC-3; The LIGO Scientific Collaboration et al. 2021), respectively, where from the Gamma-ray Coordinates Network there were 31 and 22 candidate events discovered during O3a and O3b, respectively. The promising candidates that are consistent with a source with $m_2 < 3 M_\odot$ and that could generate electromagnetic emission are GW190425, GW190426_152155, and GW190814 in GWTC-2 (Abbott et al. 2021) and GW191219_163120,

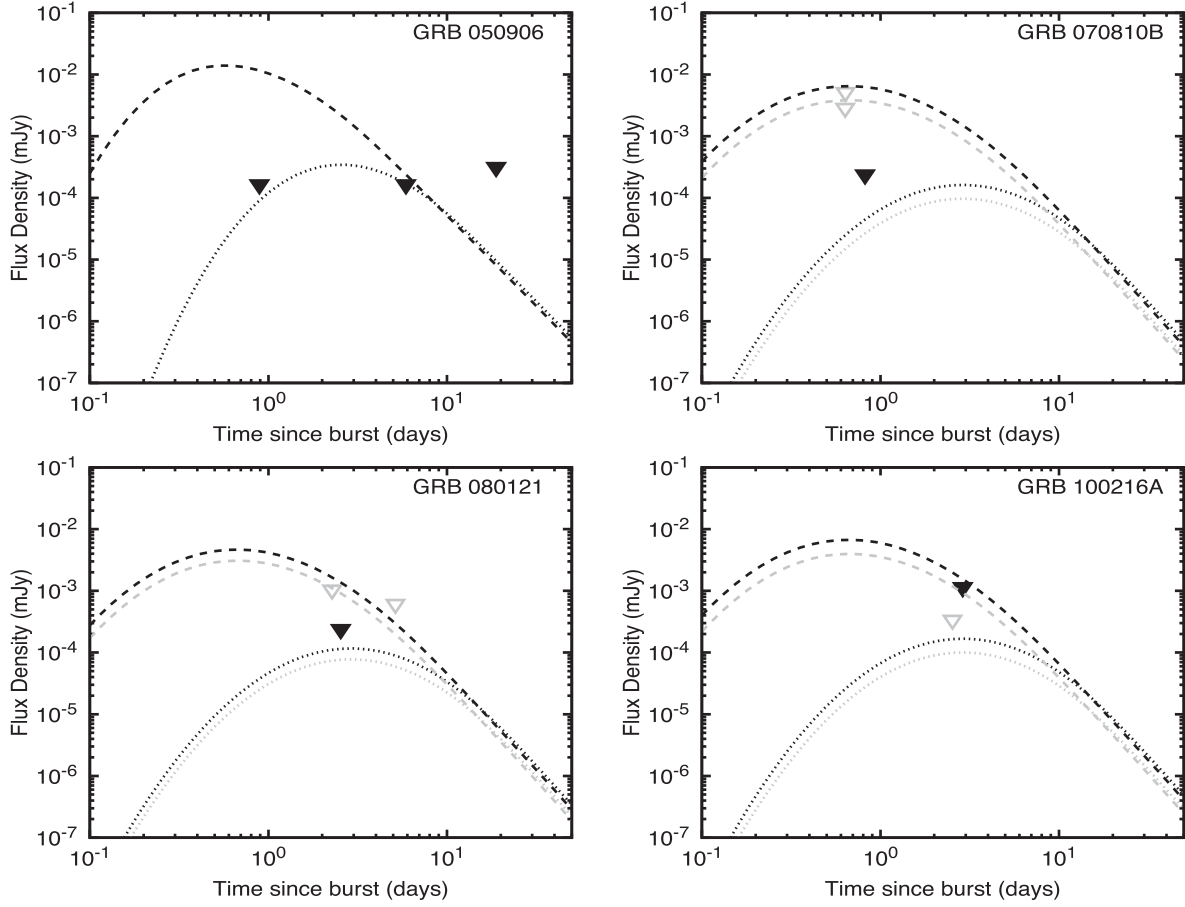


Figure 15. Optical (u - and r -band) upper limits for GRB 050906, GRB 070810B, GRB 080121, and GRB 100216A with a set of synchrotron light curves evolving in a constant-density medium. The dashed and dotted lines are shown with $n = 1 \text{ cm}^{-3}$ and $n = 10^{-2} \text{ cm}^{-3}$, respectively. The parameter values used are $E = 5 \times 10^{50} \text{ erg}$, $\theta_j = 3^\circ$, $\theta_{\text{obs}} = 15^\circ$, $\Gamma = 100$, $\varepsilon_e = 0.3$, $p = 2.5$, $\zeta_e = 1.0$, and $\varepsilon_B = 10^{-4}$. Upper limits are taken from Dichiara et al. (2020).

Table 6
Values Used in the Synchrotron Light Curves of the Closest sGRBs Detected by the Swift Satellite

Parameters	GRB 050906	GRB 070810B	GRB 080121	GRB 100216A
E (10^{50} erg)	5.00 5.00	5.00 5.00	5.00 5.00	5.00 5.00
n (10^{-2} cm^{-3})	1.00 100.00	1.00 100.00	1.00 100.00	1.00 100.00
p	2.50 2.50	2.50 2.50	2.50 2.50	2.50 2.50
ε_B (10^{-4})	1.00 1.00	1.00 1.00	1.00 1.00	1.00 1.00
ε_e (10^{-1})	3.00 3.00	3.00 3.00	3.00 3.00	3.00 3.00
Γ	100.0 100.0	100.0 100.0	150.0 100.0	80.0 100.0
θ_j ($^\circ$)	3.00 3.00	3.00 3.00	3.00 3.00	3.00 3.00
θ_{obs} ($^\circ$)	15.00 15.00	15.00 15.00	15.00 15.00	15.00 15.00

Table 7
Quantities Derived of the Promising GW Events from GWTC-2 and GWTC-3

	Event	SID	Mass 1 (M_{\odot})	Mass 2 (M_{\odot})	z	References
GWTC-2	GW190425	S190425z	$3.4_{-0.1}^{+0.3}$	$1.44_{-0.02}^{+0.02}$	$0.03_{-0.02}^{+0.01}$	(a), (b), (c)
	GW190426_152155	S190426c	$5.7_{-2.3}^{+3.9}$	$1.5_{-0.5}^{+0.8}$	$0.08_{-0.03}^{+0.04}$	(d), (e), (f), (g)
	GW190814	S190814bv	$23.2_{-1.0}^{+1.1}$	$2.59_{-0.09}^{+0.08}$	$0.05_{-0.010}^{+0.009}$	(h), (i), (j), (k), (l), (m)
GWTC-3	GW191219_163120		$31.1_{-2.8}^{+2.2}$	$1.17_{-0.06}^{+0.07}$	$0.11_{-0.03}^{+0.05}$	(n)
	GW200105_162426	S200105ae	$9.0_{-1.7}^{+1.7}$	$1.91_{-0.24}^{+0.33}$	$0.06_{-0.02}^{+0.02}$	(o)
	GW200115_042309	S200115j	$5.9_{-2.5}^{+2.0}$	$1.44_{-0.29}^{+0.85}$	$0.05_{-0.010}^{+0.009}$	(p), (q)
	GW200210_092254		$24.1_{-4.6}^{+7.5}$	$2.83_{-0.42}^{+0.47}$	$0.19_{-0.06}^{+0.08}$	(n)

References: (a) Breeveld et al. (2019), (b) Tohuvavohu et al. (2019a), (c) Bochenek (2019), (d) Rhodes et al. (2019), (e) Corsi et al. (2019), (f) Bochenek et al. (2019), (g) Tohuvavohu et al. (2019b), (h) LIGO Scientific Collaboration & Virgo Collaboration (2019), (i) Andreoni et al. (2020), (j) Dobie et al. (2019), (k) Watson et al. (2020), (l) Ackley et al. (2020), (m) Vieira et al. (2020), (n) The LIGO Scientific Collaboration et al. (2021), (o) Ridnaia et al. (2020a), (p) Sakamoto & Swift Team (2020), and (q) Ridnaia et al. (2020b).

GW200105_162426, GW200115_042309, and GW200210_092254 in GWTC-3 (The LIGO Scientific Collaboration et al. 2021). Table 7 enumerates the main characteristics of these candidates.

Figure 16 shows the multiwavelength upper limits of GW events in GWTC-2 and GWTC-3 consistent with a source with $m_2 < 3 M_{\odot}$ and that could generate electromagnetic emission and the synchrotron light curves from an off-axis outflow decelerating in a constant-density medium with $n = 1 \text{ cm}^{-3}$ (left panels) and 10^{-2} cm^{-3} (right panels). The synchrotron light curves are presented at 1 keV (green), the R band (brown; from Becerra et al. 2021a), and 3 GHz (red). The parameter values used are $E = 5 \times 10^{50} \text{ erg}$, $\theta_j = 3^\circ$, $\theta_{\text{obs}} = 6^\circ$, $\Gamma = 100$, $\varepsilon_e = 0.1$, $p = 2.5$, $\zeta_e = 1.0$, and $\varepsilon_B = 10^{-2}$. The left panels associated with the S190425z, S190426c, S190814bv, and S200115j events show that a uniform density is ruled out for $n = 1 \text{ cm}^{-3}$ but not for $n = 10^{-2} \text{ cm}^{-3}$. For instance, we can note that in the panel related to S190426c, the synchrotron emission at 1 keV, the R band, and 3 GHz is above the upper limits around ~ 1 day for $n = 1 \text{ cm}^{-3}$, and in the panel associated with S190814bv, the synchrotron flux at the R band and 3 GHz is above the upper limits, but not at 1 keV. The value of the constant-density medium ruled out in our model is consistent with the densities derived by Dobie et al. (2019), Ackley et al. (2020), and Gomez et al. (2019) using distinct off-axis jet models. We need further observations on different timescales and energy bands to derive tighter constraints.

5. Conclusions

We have extended the synchrotron off-axis model presented in Fraija & Lopez-Camara (2019b) initially proposed to describe the multiwavelength afterglow observations in GRB 170817A. In the current model, we have considered (i) the circumburst external medium as stratified with a profile density $\propto r^{-k}$ with k in the range of $0 \leq k \leq 3$, (ii) the synchrotron radiation in the self-absorption regime, (iii) the afterglow emission during the transition from off-axis to on-axis before the lateral expansion phase (relativistic phase), (iv) the hydrodynamical evolution computed by numerical simulations, and (v) a fraction of electrons accelerated by the shock

front. The time evolution of the Doppler factor, the half-opening angle, the bulk Lorentz factor, and the deceleration radius computed by numerical simulations are in good agreement with those derived with an analytical approach. The advantage of this general approach (with a density profile $A_k \propto r^{-k}$) is that this model allows us to take into account not only both a homogeneous ($k = 0$) and a wind-like ($k = 2$) medium but also regions with nonstandard stratification parameters, such as $k = 1.0, 1.5$, or 2.5 .

We have calculated the synchrotron light curves and presented the closure relations in a stratified environment, including the self-absorption regime for all cooling conditions during the coasting, deceleration (off- and on-axis emission), and post-jet break decay phases. We have noted that a break is expected around the transition between fast- and slow-cooling regimes during the deceleration phase when the afterglow emission seems off-axis, but not during other stages. We have analyzed the behavior of the flux for different parameters of the density distribution. We have noticed that the behavior during the relativistic phase approaches flatness as the stratification parameter is raised. On the other hand, we have shown that the time evolution of the light curves after the jet break is independent of k , so this model gives freedom to explain the early-time evolution of the radiation while keeping the long-time results invariant. Furthermore, we have derived the change of the density parameter in the entire phase. We have shown that, in general, during the coasting and deceleration phases, when the afterglow emission seems off-axis, a transition between different environments cannot be detected, contrary to the post-jet break and deceleration phases with on-axis emission. The synchrotron fluxes do not depend on the density parameter when they are observed at the lowest and highest frequencies when the afterglow emission seems off- and on-axis, respectively. During the post-jet break phase, any transition between a stratified environment and density-constant medium will be better observed in low frequencies, such as radio wavelengths.

In particular, we have applied our model to describe the delayed nonthermal emission observed in a sample of bursts with evidence of off-axis emission. In accordance with the best-fit values for sGRBs, we found that (i) the constant-density

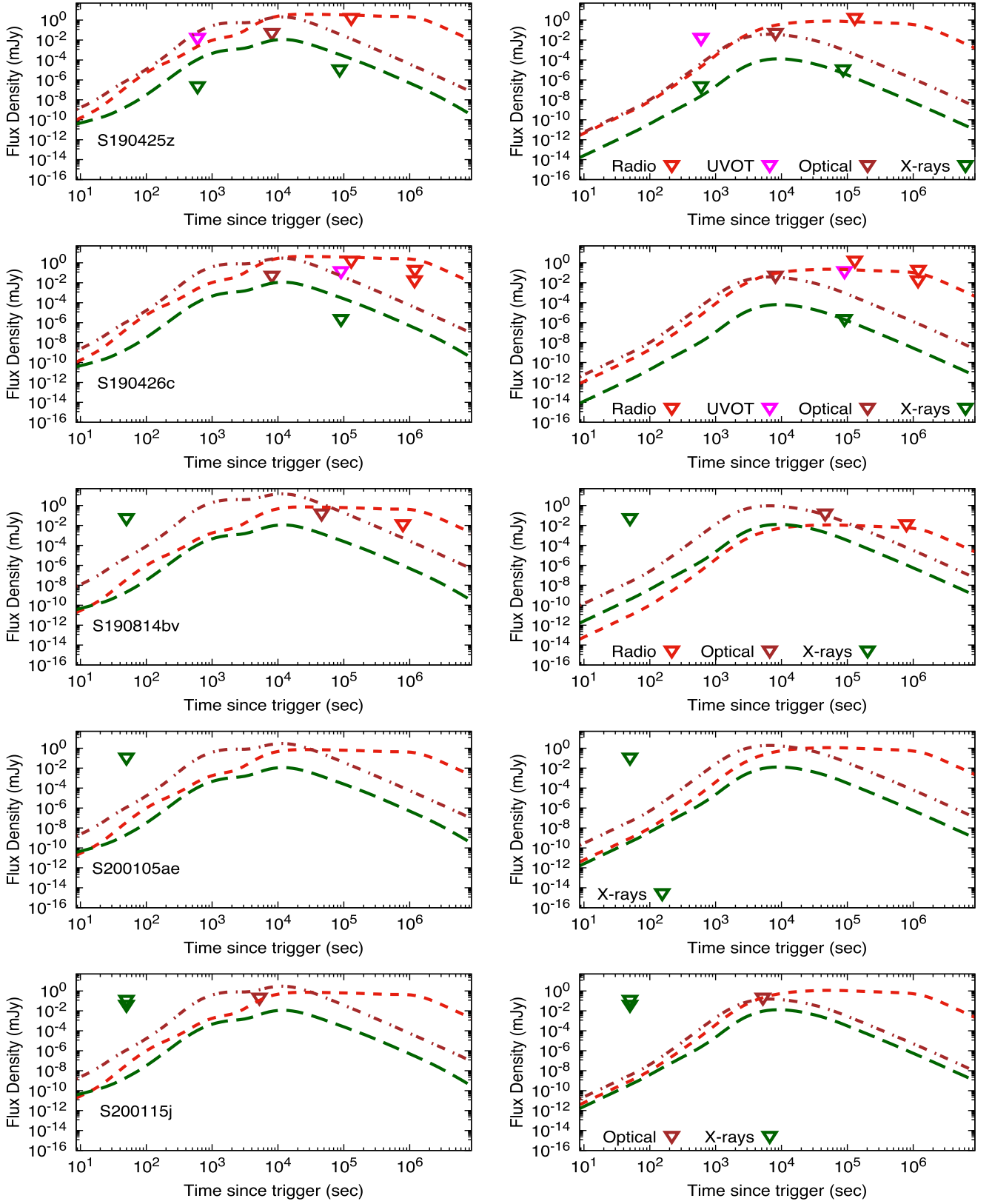


Figure 16. Promising GW events in O3 that could generate electromagnetic emission with the synchrotron light curves evolving in a constant-density medium with $n = 1 \text{ cm}^{-3}$ (left panels) and $n = 10^{-2} \text{ cm}^{-3}$ (right panels), which are decelerating in a constant-density medium. The synchrotron light curves are shown in the X-ray (1 keV; green), optical (R band; brown), and radio (3 GHz; red) bands. The parameter values used are $E = 5 \times 10^{50} \text{ erg}$, $\theta_j = 3^\circ$, $\theta_{\text{obs}} = 6^\circ$, $\Gamma = 100$, $\varepsilon_e = 0.1$, $p = 2.5$, $\zeta_e = 1.0$, and $\varepsilon_B = 10^{-2}$. Upper limits are taken from Bochenek (2019); Breeveld et al. (2019); Corsi et al. (2019); Mooley et al. (2019); Palmer et al. (2019); Rhodes et al. (2019); Ridnaia et al. (2020a, 2020b); Sakamoto & Swift Team (2020); Thakur et al. (2020); Tohuvavohu et al. (2019a, 2019b).

medium required to model the multiwavelength observations is low ($10^{-2} \text{ cm}^{-3} \leq n \leq 0.4 \text{ cm}^{-3}$), indicating that the central engine is located in a low-density circumstellar medium; (ii) the spectral indexes of the shocked electrons ($2.1 \leq p \leq 2.3$) are in the range of those reported after the description of the afterglow observations (see, e.g., Kumar & Zhang 2015; Fraija et al. 2017; Becerra et al. 2019a, 2019b, 2019c, 2021b); and (iii) the half-opening angles ($1.5^\circ \leq \theta_j \leq 6.6^\circ$), bulk Lorentz factors ($130 \leq \Gamma \leq 450$), and equivalent kinetic energies ($0.2 \text{ erg} \leq E \leq 5.7 \times 10^{52} \text{ erg}$) provide evidence of narrowly collimated outflow expanding into a constant-density environment. The previous results confirm that the multiwavelength observations are emitted from the GRB afterglow and indicate a merger of compact objects (two NSs or NS–BH) as possible progenitors of these bursts. The low-density medium agrees with the larger offsets of sGRBs compared with IGRBs. Regarding SN 2020bvc, we found that an atypical stratification parameter of $k = 1.5$ is required, supporting the CC SN scenario. The best-fit values of the half-opening angle $2.121_{-0.079}^{+0.078} \text{ }^\circ$, viewing angle $12.498_{-0.281}^{+0.268} \text{ }^\circ$, equivalent kinetic energy $2.38_{-0.10}^{+0.11} \times 10^{51} \text{ erg}$, and bulk Lorentz factor $2.291_{-0.100}^{+0.100} \times 10^2$ provide evidence of the scenario of off-axis GRB afterglow.

We have applied the current model to provide constraints on the possible afterglow emission using multiwavelength upper limits associated with the closest Swift-detected sGRBs ($< 200 \text{ Mpc}$) and the promising GW events. We have shown that the value of the constant-density medium is ruled out, which is consistent with the mean value of densities reported for sGRBs (e.g., see Berger 2014) and those derived by the S190814bv event (e.g., see Dobie et al. 2019; Gomez et al. 2019; Ackley et al. 2020) using different models. To derive tighter constraints, further observations on timescales from months to years post–merger phase are required.

We would like to express our gratitude to the anonymous referee for the careful reading of the manuscript and insightful recommendations that helped improve the paper’s quality and clarity. We thank Rodolfo Barniol Duran, Tanmoy Laskar, Paz Beniamini, and Bing Zhang for useful discussions. N.F. acknowledges financial support from UNAM-DGAPA-PAPIIT through grant IN106521. R.L.B. acknowledges support from CONACyT postdoctoral fellowships and DGAPA/UNAM IG100820 and IN105921.

Appendix

Analytical Synchrotron Afterglow Model from an Off-axis Outflow

A.1. Coasting Phase

During the coasting phase, the bulk Lorentz factor is constant. The minimum and the cooling electron Lorentz factor are given by

$$\begin{aligned} \gamma_m &= \gamma_m^0 g(p) \varepsilon_{e,-1} \zeta_e^{-1} \Gamma_{2.5}, \\ \gamma_c &= \gamma_c^0 \left(\frac{1+z}{1.022} \right)^{1-k} (1+Y)^{-1} \varepsilon_{B,-4} A_k^{-1} \\ &\quad \times \Gamma_{2.5}^{-1} f(\Delta\theta)^{k-1} t^{k-1}, \end{aligned}$$

where $f(\Delta\theta) \equiv \frac{1}{1-\mu\beta}$. The synchrotron spectral breaks and maximum flux are

$$\begin{aligned} \nu_m &\simeq \nu_m^0 \left(\frac{1+z}{1.022} \right)^{\frac{k-2}{2}} g(p)^2 \zeta_e^{-2} \varepsilon_{e,-1}^2 \varepsilon_{B,-4}^{\frac{1}{2}} \\ &\quad \times A_k^{\frac{1}{2}} f(\Delta\theta)^{\frac{2-k}{2}} \Gamma_{2.5}^2 t^{-\frac{k}{2}} \\ \nu_c &\simeq \nu_c^0 \left(\frac{1+z}{1.022} \right)^{\frac{2-3k}{2}} (1+Y)^{-2} \varepsilon_{B,-4}^{-\frac{3}{2}} \\ &\quad \times A_k^{-\frac{3}{2}} f(\Delta\theta)^{\frac{3k-2}{2}} \Gamma_{2.5}^{-2} t^{\frac{3k-4}{2}} \\ F_{\max} &\simeq F_{\max}^0 \left(\frac{1+z}{1.022} \right)^{\frac{3k-2}{2}} \zeta_e \varepsilon_{B,-4}^{\frac{1}{2}} \\ &\quad \times A_k^{\frac{3}{2}} f(\Delta\theta)^{\frac{12-3k}{2}} d_{z,28.3}^{-2} \Gamma_{2.5}^{-2} t^{\frac{6-3k}{2}}. \end{aligned} \quad (\text{A1})$$

In the self-absorption regime, the spectral breaks are

$$\begin{aligned} \nu_{a,1} &\simeq \nu_{a,1}^0 g(p)^{-1} \left(\frac{1+z}{1.022} \right)^{\frac{4(k-2)}{5}} \zeta_e A_k^{\frac{4}{5}} \varepsilon_{e,-1}^{-1} \varepsilon_{B,-4}^{\frac{1}{5}} \\ &\quad \times f(\Delta\theta)^{\frac{4(2-k)}{5}} \Gamma_{2.5}^{-\frac{8}{5}} t^{\frac{3-4k}{5}} \\ \nu_{a,2} &\simeq \nu_{a,2}^0 g(p)^{\frac{2(p-1)}{p+4}} \left(\frac{1+z}{1.022} \right)^{\frac{(k-2)(p+6)}{2(p+4)}} \zeta_e^{\frac{2(1-p)}{p+4}} \\ &\quad \times A_k^{\frac{p+6}{2(p+4)}} \varepsilon_{B,-4}^{\frac{p+2}{2(p+4)}} \varepsilon_{e,-1}^{\frac{2(p-1)}{p+4}} \\ &\quad \times f(\Delta\theta)^{\frac{(2-k)(p+6)}{2(p+4)}} \Gamma_{2.5}^{\frac{2(p-2)}{p+4}} t^{\frac{4-k(p+6)}{2(p+4)}} \\ \nu_{a,3} &\simeq \nu_{a,3}^0 \left(\frac{1+z}{1.022} \right)^{\frac{9k-13}{5}} (1+Y) \\ &\quad \times A_k^{\frac{9}{5}} \varepsilon_{B,-4}^{\frac{6}{5}} f(\Delta\theta)^{\frac{13-9k}{5}} \Gamma_{2.5}^{\frac{2}{5}} t^{\frac{8-9k}{5}}. \end{aligned} \quad (\text{A2})$$

Given the spectral breaks and maximum flux from Equations (A1) and (A2), the evolution of synchrotron light curves through the spectral and temporal indexes is listed in Table 1. Similarly, the closure relations for each cooling condition during the coasting phase are reported in Table 2.

A.2. Deceleration Phase (Off-axis Afterglow Emission)

During the deceleration phase before afterglow emission enters the observer’s field of view, the bulk Lorentz factor is given by Equation (4). The minimum and cooling electron Lorentz factors are given by

$$\begin{aligned} \gamma_m &= \gamma_m^0 g(p) \left(\frac{1+z}{1.022} \right)^{\frac{3-k}{2}} \zeta_e^{-1} A_k^{-\frac{1}{2}} \varepsilon_{e,-1} \theta_{j,10}^{-1} \\ &\quad \times \Delta\theta_{15}^{3-k} E_{54}^{\frac{1}{2}} t_{6.7}^{\frac{k-3}{2}} \\ \gamma_c &= \gamma_c^0 \left(\frac{1+z}{1.022} \right)^{-\frac{k+1}{2}} A_k^{-\frac{1}{2}} (1+Y)^{-1} \varepsilon_{B,-4}^{-1} \theta_{j,5} \\ &\quad \times \Delta\theta_{15}^{-(k+1)} E_{54}^{-\frac{1}{2}} t_{6.7}^{\frac{k+1}{2}}, \end{aligned}$$

which correspond to a comoving magnetic field given by $B' \propto \left(\frac{1+z}{1.022} \right)^{\frac{3}{2}} \varepsilon_{B,-4}^{\frac{1}{2}} \theta_{j,10}^{-1} \Delta\theta_{15}^3 E_{54}^{\frac{1}{2}} t_{6.7}^{-\frac{3}{2}}$. The synchrotron spectral

breaks and maximum flux can be written as

$$\begin{aligned}
\nu_m &= \nu_m^0 \left(\frac{1+z}{1.022} \right)^{\frac{4-k}{2}} \zeta_e^{-2} A_k^{-\frac{1}{2}} \varepsilon_{e,-1}^2 \varepsilon_{B,-4}^{\frac{1}{2}} \theta_{j,10}^{-2} \\
&\quad \times \Delta \theta_{15}^{4-k} E_{54}^{\frac{k-6}{2}} t_{6,7}^{\frac{k-6}{2}} \\
\nu_c &= \nu_c^0 \left(\frac{1+z}{1.022} \right)^{-\frac{k+4}{2}} A_k^{-\frac{1}{2}} (1+Y)^{-2} \varepsilon_{B,-4}^{-\frac{3}{2}} \theta_{j,10}^2 \\
&\quad \times \Delta \theta_{15}^{-(k+4)} E_{54}^{-1} t_{6,7}^{\frac{k+2}{2}} \\
F_{\max} &= F_{\max}^0 \left(\frac{1+z}{1.022} \right)^{\frac{5k-8}{2}} \zeta_e A_k^{\frac{5}{2}} \varepsilon_{B,-4}^{\frac{1}{2}} d_{z,28.3}^{-2} \theta_{j,10}^2 \\
&\quad \times \Delta \theta_{15}^{5k-18} E_{54}^{-1} t_{6,7}^{\frac{12-5k}{2}}.
\end{aligned} \tag{A3}$$

In the self-absorption regime, the spectral breaks are given by

$$\begin{aligned}
\nu_{a,1} &\simeq \nu_{a,1}^0 g(p)^{-1} \left(\frac{1+z}{1.022} \right)^{\frac{4(2k-5)}{5}} \zeta_e A_k^{\frac{8}{5}} \varepsilon_{e,-1}^{-1} \varepsilon_{B,-4}^{\frac{1}{5}} \theta_{j,10}^{\frac{8}{5}} \\
&\quad \times \Delta \theta_{15}^{\frac{8(2k-5)}{5}} E_{54}^{-\frac{4}{5}} t_{6,7}^{\frac{15-8k}{5}} \\
\nu_{a,2} &\simeq \nu_{a,2}^0 g(p)^{\frac{2(1-p)}{p+4}} \left(\frac{1+z}{1.022} \right)^{-\frac{24-10k-4p+kp}{2(p+4)}} \zeta_e^{\frac{2(1-p)}{p+4}} \\
&\quad \times A_k^{\frac{10-p}{2(p+4)}} \varepsilon_{B,-4}^{\frac{p+2}{2(p+4)}} \varepsilon_{e,-1}^{\frac{2(p-1)}{p+4}} \theta_{j,10}^{\frac{2(2-p)}{p+4}} \\
&\quad \times \Delta \theta_{15}^{\frac{4(p-6)-k(p-10)}{p+4}} E_{54}^{\frac{p-2}{p+4}} t_{6,7}^{\frac{16-10k-6p+kp}{2(p+4)}} \\
\nu_{a,3} &\simeq \nu_{a,3}^0 \left(\frac{1+z}{1.022} \right)^{\frac{2(4k-5)}{5}} (1+Y) A_k^{\frac{8}{5}} \varepsilon_{B,-4}^{\frac{6}{5}} \theta_{j,10}^{-\frac{2}{5}} \\
&\quad \times \Delta \theta_{15}^{\frac{4(4k-5)}{5}} E_{54}^{\frac{1}{5}} t_{6,7}^{\frac{5-8k}{5}}.
\end{aligned} \tag{A4}$$

Given the spectral breaks and maximum flux from Equations (A3) and (A4), the evolution of synchrotron light curves through the spectral and temporal indexes is listed in Table 1. Similarly, the closure relations for each cooling condition during the deceleration phase before the afterglow emission is seen off-axis are reported in Table 2.

A.3. Deceleration Phase (On-axis Afterglow Emission)

As the bulk Lorentz factor becomes $\Gamma \sim \Delta\theta^{-1}$, the afterglow emission becomes on-axis, being in our field of view. For the adiabatic regime, the bulk Lorentz factor is given by Equation (5). As $\Delta\theta$ becomes close to zero ($\Delta\theta \approx 0$), the bulk Lorentz factor during the relativistic phase $\Gamma \approx 1/2(1-\beta)$; therefore, the Doppler factor can be approximated to $\delta_D \approx 2\Gamma$. The minimum and cooling electron Lorentz factors are given by Fraija et al. (2019e, 2019f)

$$\begin{aligned}
\gamma_m &= \gamma_m^0 g(p)^2 \left(\frac{1+z}{1.022} \right)^{\frac{3-k}{2(4-k)}} \zeta_e^{-1} A_k^{-\frac{1}{2(4-k)}} \\
&\quad \times \varepsilon_{e,-1} E_{54}^{\frac{1}{2(4-k)}} t_{6,7}^{\frac{k-3}{2(4-k)}} \\
\gamma_c &= \gamma_c^0 \left(\frac{1+z}{1.022} \right)^{-\frac{k+1}{2(4-k)}} A_k^{-\frac{5}{2(4-k)}} (1+Y)^{-1} \\
&\quad \times \varepsilon_{B,-4}^{-1} E_{54}^{\frac{2k-3}{2(4-k)}} t_{6,7}^{\frac{k+1}{2(4-k)}},
\end{aligned}$$

which correspond to a comoving magnetic field given by $B' \propto \left(\frac{1+z}{1.022} \right)^{\frac{3}{2(4-k)}} A_k^{\frac{3}{2(4-k)}} \varepsilon_{B,-4}^{\frac{1}{2}} E_{54}^{\frac{1-k}{2(4-k)}} t_{6,7}^{-\frac{3}{2(4-k)}}$. The synchrotron spectral breaks and maximum flux can be written as

$$\begin{aligned}
\nu_m &= \nu_m^0 g(p)^2 \left(\frac{1+z}{1.022} \right)^{\frac{1}{2}} \zeta_e^{-2} \varepsilon_{e,-1}^2 \varepsilon_{B,-4}^{\frac{1}{2}} E_{54}^{\frac{1}{2}} t_{6,7}^{-\frac{3}{2}} \\
\nu_c &= \nu_c^0 \left(\frac{1+z}{1.022} \right)^{-\frac{k+4}{2(4-k)}} A_k^{-\frac{4}{4-k}} (1+Y)^{-2} \\
&\quad \times \varepsilon_{B,-4}^{-\frac{3}{2}} E_{54}^{\frac{3k-4}{2(4-k)}} t_{6,7}^{\frac{3k-4}{2(4-k)}} \\
F_{\max} &= F_{\max}^0 \left(\frac{1+z}{1.022} \right)^{\frac{16-3k}{2(4-k)}} \zeta_e A_k^{\frac{2}{4-k}} \\
&\quad \times \varepsilon_{B,-4}^{\frac{1}{2}} d_{z,28.3}^{-2} E_{54}^{\frac{8-3k}{2(4-k)}} t_{6,7}^{-\frac{k}{2(4-k)}}.
\end{aligned} \tag{A5}$$

In the self-absorption regime, the spectral breaks are given by

$$\begin{aligned}
\nu_{a,1} &\simeq \nu_{a,1}^0 g(p)^{-1} \left(\frac{1+z}{1.022} \right)^{\frac{4(2k-5)}{5(4-k)}} \zeta_e A_k^{\frac{12}{5(4-k)}} \varepsilon_{e,-1}^{-1} \varepsilon_{B,-4}^{\frac{1}{5}} \\
&\quad \times E_{54}^{\frac{4(1-k)}{5(4-k)}} t_{6,7}^{-\frac{3k}{5(4-k)}} \\
\nu_{a,2} &\simeq \nu_{a,2}^0 g(p)^{\frac{2(1-p)}{p+4}} \left(\frac{1+z}{1.022} \right)^{\frac{4(p-6)-k(p-10)}{2(4-k)(p+4)}} \zeta_e^{\frac{2(1-p)}{p+4}} \\
&\quad \times A_k^{\frac{8}{(4-k)(p+4)}} \varepsilon_{B,-4}^{\frac{p+2}{2(p+4)}} \varepsilon_{e,-1}^{\frac{2(p-1)}{p+4}} \\
&\quad \times E_{54}^{\frac{4(p+2)-k(p+6)}{2(4-k)(p+4)}} t_{6,7}^{-\frac{4(3p+2)+k(2-3p)}{2(4-k)(p+4)}} \\
\nu_{a,3} &\simeq \nu_{a,3}^0 \left(\frac{1+z}{1.022} \right)^{\frac{2(4k-5)}{5(4-k)}} (1+Y) A_k^{\frac{22}{5(4-k)}} \\
&\quad \times \varepsilon_{B,-4}^{\frac{6}{5}} E_{54}^{\frac{14-9k}{5(4-k)}} t_{6,7}^{-\frac{10+3k}{5(4-k)}}.
\end{aligned} \tag{A6}$$

Given the spectral breaks and maximum flux from Equations (A5) and (A6), the evolution of synchrotron light curves through the spectral and temporal indexes is listed in Table 1. Similarly, the closure relations for each cooling condition during the deceleration phase once the afterglow emission is in the observer's field of view are reported in Table 2.

A.4. Post-Jet Break Decay Phase

The bulk Lorentz factor decelerating in the stratified environment far away from the progenitor becomes $\Gamma \sim \theta_j^{-1}$ (Sari et al. 1999; Granot et al. 2002, 2018). During the post-jet break decay phase, the bulk Lorentz factor evolves following Equation (6). The minimum and cooling electron Lorentz factors are given by

$$\begin{aligned}
\gamma_m &= \gamma_m^0 g(p) \left(\frac{1+z}{1.022} \right)^{\frac{1}{2}} \zeta_e^{-1} \varepsilon_{e,-1} A_k^{\frac{1}{2(k-3)}} E_{54}^{-\frac{1}{2(k-3)}} t_{6,7}^{-\frac{1}{2}} \\
\gamma_c &= \gamma_c^0 \left(\frac{1+z}{1.022} \right)^{-\frac{1}{2}} (1+Y)^{-1} \varepsilon_{B,-4}^{-1} A_k^{\frac{3}{2(k-3)}} E_{54}^{\frac{3-2k}{2(k-3)}} t_{6,7}^{\frac{1}{2}}.
\end{aligned}$$

In this case, the synchrotron spectral breaks and maximum flux become

$$\begin{aligned}\nu_m &\simeq \nu_m^0 g(p)^2 \left(\frac{1+z}{1.022} \right) \zeta_e^{-2} A_k^{\frac{1}{2(k-3)}} \varepsilon_{e,-1}^2 \varepsilon_{B,-4}^{\frac{1}{2}} E_{54}^{\frac{k-4}{2(k-3)}} t_7^{-2} \\ \nu_c &\simeq \nu_c^0 \left(\frac{1+z}{1.022} \right)^{-1} A_k^{\frac{5}{2(k-3)}} \varepsilon_{B,-4}^{-\frac{3}{2}} (1+Y)^{-2} E_{54}^{\frac{4-3k}{2(k-3)}} t_7 \\ F_{\max} &\simeq F_{\max}^0 \left(\frac{1+z}{1.022} \right)^3 \zeta_e A_k^{\frac{1}{2(k-3)}} \varepsilon_{B,-4}^{\frac{1}{2}} d_{z,28.3}^{-2} \\ &\quad \times E_{54}^{\frac{8-3k}{2(k-3)}} t_7^{-1}.\end{aligned}\tag{A7}$$








Taking into account the self-absorption regime, the spectral breaks are given by

$$\begin{aligned}\nu_{a,1} &= \nu_{a,1}^0 g(p)^{-1} \left(\frac{1+z}{1.022} \right)^{-\frac{4}{5}} \zeta_e A_k^{\frac{8}{5(3-k)}} \varepsilon_{e,-1}^{-1} \varepsilon_{B,-4}^{\frac{1}{5}} \\ &\quad \times E_{54}^{\frac{4(k-1)}{5(k-3)}} t_7^{-\frac{1}{5}} \\ \nu_{a,2} &= \nu_{a,2}^0 g(p)^{\frac{2(1-p)}{p+4}} \left(\frac{1+z}{1.022} \right)^{\frac{p-2}{p+4}} \zeta_e^{\frac{2(1-p)}{p+4}} \\ &\quad \times A_k^{\frac{p-10}{2(p+4)(k-3)}} \varepsilon_{B,-4}^{\frac{p+2}{2(p+4)}} \varepsilon_{e,-1}^{\frac{2(p-1)}{p+4}} \\ &\quad \times E_{54}^{\frac{k(p+6)-4(p+2)}{2(p+4)(k-3)}} t_7^{-\frac{2(p+1)}{p+4}}.\end{aligned}\tag{A8}$$

Given the spectral breaks and maximum flux from Equations (A7) and (A8), the evolution of synchrotron light curves through the spectral and temporal indexes is listed in Table 1. Similarly, the closure relations for each cooling condition during the post-jet break decay phase are reported in Table 2.

The terms γ_m^0 , γ_c^0 , ν_m^0 , ν_c^0 , F_{\max}^0 , $\nu_{a,1}^0$, $\nu_{a,2}^0$, and $\nu_{a,3}^0$ during the coasting, deceleration (off- and on-axis emission), and post-jet break decay phases are shown in Table 3 for $k=0, 1, 1.5$, and 2.

ORCID iDs

N. Fraija  <https://orcid.org/0000-0002-0173-6453>
A. Galvan-Gamez  <https://orcid.org/0000-0001-5193-3693>
B. Betancourt Kamenetskaia  <https://orcid.org/0000-0002-2516-5739>
M. G. Dainotti  <https://orcid.org/0000-0003-4442-8546>
S. Dichiara  <https://orcid.org/0000-0001-6849-1270>
P. Veres  <https://orcid.org/0000-0002-2149-9846>
R. L. Becerra  <https://orcid.org/0000-0002-0216-3415>

References

Abbott, B. P., Abbott, R., Abbott, T. D., et al. 2017a, *PhRvL*, **119**, 161101
Abbott, B. P., Abbott, R., Abbott, T. D., et al. 2017b, *ApJL*, **848**, L12
Abbott, B. P., Abbott, R., Abbott, T. D., et al. 2017, *ApJ*, **848**, L13
Abbott, R., Abbott, T. D., Abraham, S., et al. 2021, *PhRvX*, **11**, 021053
Ackley, K., Amati, L., Barbieri, C., et al. 2020, *A&A*, **643**, A113
Alexander, K. D., Berger, E., Fong, W., et al. 2017, *ApJ*, **848**, L21
Alexander, K. D., Margutti, R., Blanchard, P. K., et al. 2018, *ApJL*, **863**, L18
Andreoni, I., Goldstein, D. A., Kasliwal, M. M., et al. 2020, *ApJ*, **890**, L31
Barthelmy, S. D., Cannizzo, J. K., Gehrels, N., et al. 2005, *ApJ*, **635**, L133
Bartos, I., Lee, K. H., Corsi, A., Márka, Z., & Márka, S. 2019, *MNRAS*, **485**, 4150
Becerra, R. L., De Colle, F., Watson, A. M., et al. 2019a, *ApJ*, **887**, 254
Becerra, R. L., Watson, A. M., Fraija, N., et al. 2019b, *ApJ*, **872**, 118

Becerra, R. L., Dichiara, S., Watson, A. M., et al. 2019c, *ApJ*, **881**, 12
Becerra, R. L., Dichiara, S., Watson, A. M., et al. 2021a, *MNRAS*, **507**, 1401
Becerra, R. L., De Colle, F., Cantó, J., et al. 2021b, *ApJ*, **908**, 39
Berger, E. 2014, *ARA&A*, **52**, 43
Blandford, R. D., & McKee, C. F. 1976, *PhFl*, **19**, 1130
Blondin, J. M., Lundqvist, P., & Chevalier, R. A. 1996, *ApJ*, **472**, 257
Bloom, J. S., & Perley, D. A. 2008, GCN, **7667**, 1
Bloom, J. S., Kulkarni, S. R., Djorgovski, S. G., et al. 1999, *Natur*, **401**, 453
Bloom, J. S., Li, W., Levan, A. J., et al. 2008, GCN, **7703**, 1
Bochenek, C. 2019, GCN, **24199**, 1
Bochenek, C., Kulkarni, S. R., McKenna, D., et al. 2019, GCN, **24253**, 1
Breeveld, A. A., Kuin, N. P. M., Marshall, F. E., et al. 2019, GCN, **24296**, 1
Brown, P. J., & Mao, J. 2008, GCN, **7675**, 1
Burns, E., Veres, P., Connaughton, V., et al. 2018, *ApJ*, **863**, L34
Cenko, S. B., Capone, J., Toy, V., et al. 2014, GCN, **16785**, 1
Chevalier, R. A. 1982, *ApJ*, **258**, 790
Chevalier, R. A. 1984, *ApJ*, **285**, L63
Corsi, A., Frail, D., Hallinan, G., Mooley, K., & Kasliwal, M. 2019, GCN, **24486**, 1
Coulter, D. A., Foley, R. J., Kilpatrick, C. D., et al. 2017, *Sci*, **358**, 1556
Cucchiara, A., Cenko, S. B., Perley, D. A., Capone, J., & Toy, V. 2014, GCN, **16774**, 1
Cucchiara, A., & Schady, P. 2008, GCN, **7217**, 1
Cummings, J. R. 2014, GCN, **16765**, 1
Cummings, J. R. 2015, GCN, **17267**, 1
Cummings, J. R., Barthelmy, S. D., Fox, D. B., et al. 2010, GCN, **10428**
Cummings, J. R., Burrows, D. N., Evans, P. A., et al. 2014, GCN, **16763**, 1
Cummings, J. R., & Palmer, M. 2008, GCN, **7209**
D'Avanzo, P., D'Elia, V., Lorenzi, V., et al. 2015, GCN, **17326**, 1
D'Avanzo, P., Campana, S., Salafia, O. S., et al. 2018, *A&A*, **613**, L1
Dichiara, S., Guidorzi, C., & Japelj, J. 2014, GCN, **16781**, 1
Dichiara, S., Troja, E., O'Connor, B., et al. 2020, *MNRAS*, **492**, 5011
Dobie, D., Stewart, A., Murphy, T., et al. 2019, *ApJ*, **887**, L13
Dobie, D., Kaplan, D. L., Murphy, T., et al. 2018, *ApJ*, **858**, L15
Duncan, R. C., & Thompson, C. 1992, *ApJ*, **392**, L9
Evans, P. A., Goad, M. R., Osborne, J. P., & Beardmore, A. P. 2016, GCN, **19837**, 1
Evans, P. A., Willingale, R., Osborne, J. P., et al. 2010, *A&A*, **519**, A102
Fan, Y., & Piran, T. 2006, *MNRAS*, **369**, 197
Fan, Y.-Z., Wei, D.-M., Zhang, F.-W., & Zhang, B.-B. 2012, *ApJ*, **755**, L6
Fong, W. 2014, GCN, **16777**, 1
Fong, W. 2015, GCN, **17288**, 1
Fong, W., Berger, E., Fox, D., & Shappee, B. J. 2015, GCN, **17333**, 1
Fong, W., Margutti, R., Chornock, R., et al. 2016, *ApJ*, **833**, 151
Fraija, N. 2015, *ApJ*, **804**, 105
Fraija, N., De Colle, F., Veres, P., et al. 2019a, *ApJ*, **871**, 123
Fraija, N., Lee, W. H., Araya, M., et al. 2017, *ApJ*, **848**, 94
Fraija, N., Lopez-Camara, D., Pedreira, A. C. C. d. E. S., et al. 2019b, *ApJ*, **884**, 71
Fraija, N., Pedreira, A. C. C. d. E. S., & Veres, P. 2019c, *ApJ*, **871**, 200
Fraija, N., Duran, R. B., Dichiara, S., & Beniamini, P. 2019d, *ApJ*, **883**, 162
Fraija, N., Dichiara, S., Caligula do E. S. Pedreira, A. C., et al. 2019e, *ApJ*, **885**, 29
Fraija, N., Dichiara, S., Pedreira, A. C. C. d. E. S., et al. 2019f, *ApJL*, **879**, L26
Fraija, N., Veres, P., Beniamini, P., et al. 2021, *ApJ*, **918**, 12
Frail, D. A., & Chandra, P. 2008, GCN, **7684**
Galama, T. J., Vreeswijk, P. M., van Paradijs, J., et al. 1998, *Natur*, **395**, 670
Gao, H., Ding, X., Wu, X.-F., Dai, Z.-G., & Zhang, B. 2015, *ApJ*, **807**, 163
Giblin, T. W., van Paradijs, J., Kouveliotou, C., et al. 1999, *ApJ*, **524**, L47
Gomez, S., Hosseinzadeh, G., Cowperthwaite, P. S., et al. 2019, *ApJ*, **884**, L55
Granut, J., Gill, R., Guetta, D., & De Colle, F. 2018, *MNRAS*, **481**, 1597
Granut, J., Panaitescu, A., Kumar, P., & Woosley, S. E. 2002, *ApJ*, **570**, L61
Guidorzi, C., & Mao, J. 2008, GCN, **7674**
Haggard, D., Nynka, M., Ruan, J. J., Evans, P., & Kalogera, V. 2018, ATel, **11242**
Hiramatsu, D., Arcavi, I., Burke, J., et al. 2020, TNSCR, **2020-403**
Ho, A. Y. Q. 2020, TNSAN, **2020-42**
Ho, A. Y. Q., Cenko, B., Perley, D., Corsi, A., & Brightman, M. 2020a, TNSAN, **2020-45**
Ho, A. Y. Q., Kulkarni, S. R., Perley, D. A., et al. 2020b, *ApJ*, **902**, 86
Hotokozaka, K., Kiuchi, K., Shibata, M., Nakar, E., & Piran, T. 2018, *ApJ*, **867**, 95
Huang, Y. F., Dai, Z. G., & Lu, T. 1999, *MNRAS*, **309**, 513
Huang, Y. F., Dai, Z. G., & Lu, T. 2000, *MNRAS*, **316**, 943
Ioka, K., & Nakamura, T. 2018, *PTEP*, **2018**, 043E02
Izzo, L., Auchettl, K., Hjorth, J., et al. 2020, *A&A*, **639**, L11

- Jin, Z.-P., Li, X., Wang, H., et al. 2018, *ApJ*, **857**, 128
- Kasliwal, M. M., Nakar, E., Singer, L. P., et al. 2017, *Sci*, **358**, 1559
- Kotak, R., Meikle, W. P. S., Adamson, A., & Leggett, S. K. 2004, *MNRAS*, **354**, L13
- Kouveliotou, C., Meegan, C. A., Fishman, G. J., et al. 1993, *ApJ*, **413**, L101
- Krimm, H., La Parola, V., de Pasquale, M., et al. 2005, GCN, **3926**, 1
- Kumar, P., Narayan, R., & Johnson, J. L. 2008, *Sci*, **321**, 376
- Kumar, P., & Zhang, B. 2015, *PhR*, **561**, 1
- Lamb, G. P., Tanvir, N. R., Levan, A. J., et al. 2019, *ApJ*, **883**, 48
- Lazzati, D., Perna, R., Morsony, B. J., et al. 2018, *PhRvL*, **120**, 241103
- Levan, A. J., Hjorth, J., Wiersema, K., & Tanvir, N. R. 2015, GCN, **17281**, 1
- Levan, A. J., Wiersema, K., Tanvir, N. R., et al. 2016, GCN, **19846**, 1
- Levan, A. J., Tanvir, N. R., Jakobsson, P., et al. 2008, *MNRAS*, **384**, 541
- Li, L.-X., & Paczyński, B. 1998, *ApJ*, **507**, L59
- Lien, A., Sakamoto, T., Barthelmy, S. D., et al. 2016, *ApJ*, **829**, 7
- LIGO Scientific Collaboration & Virgo Collaboration 2019, GCN, **25324**, 1
- Lü, H.-J., Zhang, H.-M., Zhong, S.-Q., et al. 2017, *ApJ*, **835**, 181
- Lü, J., Zou, Y.-C., Lei, W.-H., et al. 2012, *ApJ*, **751**, 49
- Lyman, J. D., Lamb, G. P., Levan, A. J., et al. 2018, *NatAs*, **2**, 751
- Mao, J., Guidorzi, C., Ukwatta, T., et al. 2008, GCNR, **138**, 1
- Margutti, R., Fong, W., Eftekhari, T., et al. 2017a, ATel, **11037**
- Margutti, R., Berger, E., Fong, W., et al. 2017b, *ApJ*, **848**, L20
- Margutti, R., Alexander, K. D., Xie, X., et al. 2018, *ApJL*, **856**, L18
- Marshall, F. E., Brown, P. J., Cummings, J. R., et al. 2007, GCN, **6743**, 1
- Metzger, B. D., Giannios, D., Thompson, T. A., Bucciantini, N., & Quataert, E. 2011, *MNRAS*, **413**, 2031
- Mooley, K. P., Nakar, E., Hotokezaka, K., et al. 2018, *Natur*, **554**, 207
- Mooley, K., Hallinan, G., Kasliwal, M., et al. 2019, GCN, **25480**, 1
- Moriya, T. J., & Tominaga, N. 2012, *ApJ*, **747**, 118
- Nakar, E., & Piran, T. 2018, *MNRAS*, **478**, 407
- Narayan, R., Paczynski, B., & Piran, T. 1992, *ApJ*, **395**, L83
- Palmer, D. M., Barthelmy, S. D., Cummings, J. R., et al. 2016, GCN, **19844**, 1
- Palmer, D. M., Barthelmy, S. D., Lien, A. Y., et al. 2019, GCN, **25341**, 1
- Panaitescu, A., & Mészáros, P. 1998, *ApJ*, **501**, 772
- Parsons, A., Sarazin, C., Barbier, L., et al. 2005, GCN, **3935**, 1
- Perley, D., Schulze, S., & Bruch, R. 2020, TNSAN, **2020-37**
- Perley, D. A., Bloom, J. S., & Li, W. 2008a, GCN, **7695**
- Perley, D. A., Bloom, J. S., & Prochaska, J. X. 2008b, GCN, **7678**
- Perley, D. A., Bloom, J. S., & Prochaska, J. X. 2008c, GCN, **7679**
- Perley, D. A., Foley, R. J., & Bloom, J. S. 2008d, GCN, **7210**
- Perley, D. A., Lai, D., Rockosi, C., & Bloom, J. S. 2008e, GCN, **7666**
- Perley, D. A., Bloom, J. S., Levan, A. J., et al. 2008f, GCN, **7749**
- Perley, D. A., Metzger, B. D., Granot, J., et al. 2009, *ApJ*, **696**, 1871
- Planck Collaboration, Ade, P. A. R., Aghanim, N., et al. 2016, *A&A*, **594**, A13
- Ramirez-Ruiz, E., Garcia-Segura, G., Salmonson, J. D., & Perez-Rendon, B. 2005, *ApJ*, **631**, 435
- Rhoads, J. E. 1999, *ApJ*, **525**, 737
- Rhodes, L., Fender, R., Williams, D., et al. 2019, GCN, **24551**, 1
- Ridnaia, A., Golenetskii, S., Aptekar, R., et al. 2020a, GCN, **26849**, 1
- Ridnaia, A., Golenetskii, S., & Aptekar, R. 2020b, GCN, **26837**, 1
- Rowlinson, A., Page, K., & Lyons, N. 2010, GCN, **10435**
- Rumyantsev, V., Biryukov, V., & Pozanenko, A. 2007, GCN, **6762**, 1
- Sakamoto, T. & Swift Team 2020, GCN, **26779**, 1
- Sakamoto, T., Troja, E., Gehrels, N., et al. 2014, GCN, **16813**, 1
- Sari, R., & Esin, A. A. 2001, *ApJ*, **548**, 787
- Sari, R., & Piran, T. 1999, *A&AS*, **138**, 537
- Sari, R., Piran, T., & Halpern, J. P. 1999, *ApJ*, **519**, L17
- Sari, R., Piran, T., & Narayan, R. 1998, *ApJ*, **497**, L17
- Savchenko, V., Ferrigno, C., Kuulkers, E., et al. 2017, *ApJ*, **848**, L15
- Siegel, M. H., Barthelmy, S. D., Burrows, D. N., et al. 2016, GCN, **19833**, 1
- Siegel, M. H., & Rowlinson, A. 2010, GCN, **10442**
- Soderberg, A. M., Chevalier, R. A., Kulkarni, S. R., & Frail, D. A. 2006, *ApJ*, **651**, 1005
- Stanbro, M. 2015, GCN, **17295**, 1
- Stanbro, M., & Meegan, C. 2016, GCN, **19843**, 1
- Stanek, K. 2020, TNSTR, **2020-381**
- Thakur, A. L., Dichiaro, S., Troja, E., et al. 2020, *MNRAS*, **499**, 3868
- The LIGO Scientific Collaboration, The Virgo Collaboration, The KAGRA Collaboration, et al. 2021, arXiv:2111.03606
- Thompson, C. 1994, *MNRAS*, **270**, 480
- Tohuvavohu, A., Evans, P. A., Kennea, J. A., et al. 2019a, GCN, **24353**, 1
- Tohuvavohu, A., Evans, P., Siegel, M., et al. 2019b, GCN, **24305**, 1
- Troja, E., & Burrows, D. N. 2008, GCN, **7224**
- Troja, E., Lipunov, V. M., Mundell, C. G., et al. 2017, *Natur*, **547**, 425
- Troja, E., Piro, L., van Eerten, H., et al. 2017, *Natur*, **551**, 71
- Troja, E., Sakamoto, T., Cenko, S. B., et al. 2016, *ApJ*, **827**, 102
- Troja, E., Ryan, G., Piro, L., et al. 2018, *NatCo*, **9**, 4089
- Troja, E., Castro-Tirado, A. J., Becerra González, J., et al. 2019a, *MNRAS*, **489**, 2104
- Troja, E., Castro-Tirado, A. J., Gonzalez, J. B., et al. 2019b, *MNRAS*, **489**, 2104
- Ukwatta, T., Stamatikos, M., Sakamoto, T., Norris, J., & Barthelmy, S. D. 2008, GCN, **7677**
- Usov, V. V. 1992, *Natur*, **357**, 472
- van Marle, A. J., Langer, N., Achterberg, A., & Garcia-Segura, G. 2006, *A&A*, **460**, 105
- Vieira, N., Ruan, J. J., Haggard, D., et al. 2020, *ApJ*, **895**, 96
- von Kienlin, A., Meegan, C., & Goldstein, A. 2017, GCN, **21520**, 1
- Wang, X.-Y., He, H.-N., Li, Z., Wu, X.-F., & Dai, Z.-G. 2010, *ApJ*, **712**, 1232
- Watson, A. M., Butler, N. R., Lee, W. H., et al. 2020, *MNRAS*, **492**, 5916
- Waxman, E. 1997, *ApJ*, **491**, L19
- Weinberg, S. 1972, *Gravitation and Cosmology: Principles and Applications of the General Theory of Relativity* (Weinheim: Wiley-VCH)
- Woosley, S. E. 1993, *ApJ*, **405**, 273
- Woosley, S. E., & Bloom, J. S. 2006, *ARA&A*, **44**, 507
- Yamazaki, R., Toma, K., Ioka, K., & Nakamura, T. 2006, *MNRAS*, **369**, 311
- Yi, S. X., Wu, X. F., & Dai, Z. G. 2013, *ApJ*, **776**, 120
- Zhang, S., Jin, Z.-P., Wang, Y.-Z., & Wei, D.-M. 2017, *ApJ*, **835**, 73